POLITECNICO DI TORINO
Repository ISTITUZIONALE

Investigating Pompeii Subsoil Using Geomatics and Geophysics Merged Analyses

Original
Investigating Pompeii Subsoil Using Geomatics and Geophysics Merged Analyses / Santoro, V., Merico, A., Sapia, V., Catanzariti, G., Materni, V., Patrucco, G., Olivito, R., Anguissola, A., Cangiano, I., Spano', A.T.. - In: ARCHAELOGICAL PROSPECTION. - ISSN 1075-2196. - ELETTRONICO. - (2026), pp. 1-28. [10.1002/arp.70066]

Availability:
This version is available at: 11583/3016427 since: 2026-10-08T07:08:59Z

Publisher:
Wiley

Published
DOI:10.1002/arp.70066

Terms of use:

This article is made available under terms and conditions as specified in the corresponding bibliographic description in the repository

Publisher copyright

(Article begins on next page)

19 November 2026

Check for updates

Archaeological Prospection

WILEY

RESEARCH ARTICLE OPEN ACCESS

Investigating Pompeii Subsoil Using Geomatics and Geophysics Merged Analyses

Valentina Santoro[1] | Antonio Merico[2] | Vincenzo Sapia[3] | Gianluca Catanzariti[4] | Valerio Materni[3] | Giacomo Patrucco[5] | Riccardo Olivito[6] | Anna Anguissola[7] | Ilaria Cangiano[8] | Antonia Spanò[1]

[1]Lab G4CH, Department of Architecture and Design (DAD), Politecnico di Torino, Torino, Italy | [2]Università degli Studi di Torino, Torino, Italy | [3]Istituto Nazionale di Geofisica e Vulcanologia, Rome, Italy | [4]3D Geoimaging, Torino, Italy | [5]Department of Theoretical and Applied Sciences (DiSTA), e-Campus University, Novedrate, Italy | [6]Scuola IMT Alti Studi Lucca, Lucca, Italy | [7]Dipartimento di Civiltà e Forme del Sapere, Università di Pisa, Pisa, Italy | [8]Parco Archeologico di Pompeii, Pompei, Italy

Correspondence: Antonio Merico (antonio.merico@unito.it)

Received: 26 June 2026 | **Revised:** 7 September 2026 | **Accepted:** 9 September 2026

Keywords: geomatics survey | GPR | multispectral imagery | *Palestra Grande* | Pompeii

ABSTRACT

The archaeological site of Pompeii represents an exceptional context for the application of non-invasive and integrated investigation methods aimed at enhancing the understanding of both exposed and buried remains. This study presents the results of multidisciplinary research conducted in the *Palestra Grande* site, a large and strategically important complex within the Archaeological Park, where no systematic archaeo-geophysical investigations had previously been carried out. Within an ongoing research agreement involving academic institutions and the Park, the study combines UAV-based geomatics analyses and near-surface geophysical investigations to support archaeological interpretation and assessment of non-excavated structures. High-resolution multispectral UAV photogrammetry was employed to generate orthophotos and spectral index maps, enabling the detection of surface anomalies potentially related to buried features. In parallel, ground penetrating radar (GPR) and electric resistivity tomography (ERT) surveys were carried out along targeted grids and profiles to investigate the shallow subsurface and to characterize the geometry and physical properties of buried anomalies. A key contribution of this work lies in the systematic comparison and integration of surface-based geomatics results and subsurface geophysical data. Visual interpretation was performed within QGIS to evaluate correspondences and discrepancies between spectral anomalies and geophysical signatures. In addition, a semi-automatic quantitative approach based on cross-correlation analysis was introduced to enhance results, which is traditionally reliant on time-consuming manual post-processing. The results demonstrate a significant degree of complementarity between geomatics and geophysical methods within the shallow subsurface, while also highlighting the different sensitivities and depth ranges of each technique achievable in this specific case study. The integrated approach provides a robust framework for identifying areas of archaeological potential, optimizing the planning of future investigations and reducing the need for invasive excavation. Overall, this study underscores the value of multidisciplinary and multi-parametric methodologies for archaeological research and heritage management in complex sites such as Pompeii.

1 | Introduction

Pompeii is an extraordinary archaeological site located near the city of Naples (Italy) that offers a glimpse into the ancient Roman civilization. Buried under layers of volcanic ash and debris after the catastrophic eruption of Mount Vesuvius in 79 AD (Sigurdsson et al. 1982), Pompeii remained remarkably preserved for centuries, providing invaluable insights into daily life during the Roman era (Aldrete 2004). Within this framework, the PRAEDIA project (Pompeian Residential Architecture:

This is an open access article under the terms of the Creative Commons Attribution License, which permits use, distribution and reproduction in any medium, provided the original work is properly cited.

© 2026 The Author(s). *Archaeological Prospection* published by John Wiley & Sons Ltd.

Environmental, Digital, Interdisciplinary Archive) was established in 2016 as a multidisciplinary initiative aimed at enhancing the study and documentation of Pompeii's residential architecture.

The project involves collaboration between the Archaeological Park of Pompeii, the Department of Civilizations and Forms of Knowledge at the University of Pisa, the IMT School for Advanced Studies Lucca, the Istituto Nazionale di Geofisica e Vulcanologia and the Politecnico di Torino.

The research programme aims to contribute to the understanding of the architectural and natural landscape of the south-eastern sector of Pompeii, corresponding to *Regio* II, from the Archaic period to the eruption of AD 79. From a broader perspective, it also extends to the first discoveries in the 18th century, the excavations and restorations carried out over the last century and recent initiatives designed to promote public access to the site. Based on an extended literature review, no archaeo-geophysical investigations have ever been performed in the *Palestra Grande* in the past. Recent archaeological excavations have been limited to the 'internal pool', i.e., *natatio* and to sectors outside the complex, specifically between the *Palestra Grande* and the amphitheatre (Iadanza and Toniolo 2022). Conversely, recent geophysical research has been conducted in the *Insula* II of the *Regio* II, namely, in the *hortus* of the *Praedia Iuliae Felicis* (Urbini et al. 2021). These investigations showed the high potential of a multiparametric geophysical approach in a complex geo-archaeological context. More specifically, the combination of magnetic and electromagnetic techniques enabled a detailed reconstruction of the shallow subsurface and revealed previously unknown structures related to ancient water-management systems, including elements of the Canal of Conte di Sarno (Marchetti et al. 2022).

As part of the ongoing research project mentioned above, the multi-disciplinary study which is the object of this paper has been conducted in the *Palestra Grande* (Figure 1). The investigations included photogrammetric acquisitions by UAV platforms, with RGB and multispectral sensors, and geophysical surveys through ground penetrating radar (GPR) and electric resistivity tomography (ERT).

Geomatics provides a wide range of methods and technologies for cultural heritage (CH) documentation and investigation, with significant applications for archaeological documentation and prospection (Stal et al. 2014; Radicioni et al. 2021; Agapiou and Skarlatos 2023). The complementary use of different surveying and sensing techniques enables accurate spatial referencing, metric and 3D documentation, spatial analysis and the integration of heterogeneous information within a common spatial framework. Within this context, aerial and remote sensing approaches have a long-established tradition in archaeology, supporting the documentation, mapping and investigation of archaeological sites and landscapes, as well as the prospection of buried features (Keiller and Crawford 1928; Schmiedt 1957; Lasaponara et al. 2007). More recently, in the last decade, advances in acquisition platforms, particularly the increasing use of unmanned aerial vehicles (UAVs), together with the parallel development of miniaturized optical



FIGURE 1 | Overview of the area investigated within the study: the Archaeological Park of Pompei is circled with a white dotted line, and the *Palestra Grande* is highlighted through a yellow box.

10990753, 0, Downloaded from https://onlinelibrary.wiley.com/doi/10.1002/arp.70066 by Valentina Santoro - Politecnico Di Torino Sist. Bibl Del Polit Di Torino , Wiley Online Library on [07/10/2026]. See the Terms and Conditions (https://onlinelibrary.wiley.com/terms-and-conditions) on Wiley Online Library for rules of use; OA articles are governed by the applicable Creative Commons License

sensors, have further expanded the application of these established approaches (Opitz and Herrmann 2018), both for the detailed recording of visible remains (Chiabrando et al. 2018; Waagen 2019) and for the detection of subsurface archaeological features, often in combination with non-destructive technologies (Salgado Carmona et al. 2020; Santoro et al. 2026). In particular, UAVs approaches enable high-resolution, accurate and cost-effective data acquisition, providing considerable flexibility for archaeological surveys (Sammartano et al. 2020; Kaimaris 2024). UAV-based photogrammetry supports the generation of three-dimensional reconstructions, digital surface models (DSMs) and orthomosaics, thereby enabling nuanced examinations of landform geometry and microtopographic variations (Lippolis et al. 2025; Shukla et al. 2023). Beyond RGB imaging, multispectral, hyperspectral and thermal sensors are increasingly employed on UAV platforms. Multispectral sensors acquire information in a relatively limited number of discrete spectral bands, covering selected portions of the electromagnetic spectrum, whereas hyperspectral sensors provide a much denser spectral sampling through numerous narrow and typically contiguous bands, enabling a more detailed characterization of spectral responses (Goetz 2009; Banerjee et al. 2020). Thermal sensors, operating in the thermal infrared (TIR) range, have likewise demonstrated significant potential for CH monitoring and archaeological detection (Hill et al. 2020; Patrucco et al. 2020). Recent studies highlight how multispectral indices and thermal anomalies—when cross-referenced with RGB imagery—can provide valuable indicators of variations in vegetation stress, soil composition or moisture retention, which in turn may correspond to subsurface structures (Kaimaris 2024). Specifically, in vegetated archaeological contexts, variations in vegetation growth and vigour caused by subsurface conditions associated with buried archaeological remains can form so-called crop marks. These may be either positive or negative, depending on how the buried features affect vegetation growth. Such variations can produce detectable spectral responses and have therefore been widely exploited in archaeological remote sensing for the identification of subsurface archaeological feature (Agapiou and Hadjimitsis 2011; Agapiou et al. 2013).

Geophysical methods represent a well-established and powerful suite of non-invasive techniques for archaeological investigations (Karaoulis et al. 2025; Balkaya et al. 2021; Orlando et al. 2019; Tejero-Andrade et al. 2018; Neubauer et al. 2002). By measuring contrasts in the physical properties of the subsurface, they allow the identification, characterization and spatial delineation of potential archaeological features with high accuracy. Among the most widely adopted methods, GPR exploits the reflection of electromagnetic waves at subsurface interfaces, enabling the detection and vertical resolution of stratified deposits and buried structures at shallow depths. Electric resistivity tomography (ERT) maps lateral and vertical contrasts in ground resistivity, proving especially valuable in complex stratigraphic contexts with deeper targets of interest. Advances in data acquisition, including multi-channel GPR arrays, have extended the spatial coverage of geophysical surveys to landscape scales, substantially increasing their operational efficiency (Corradini et al. 2022; Forte et al. 2022; Filzwieser et al. 2017). At the same time, developments in processing and visualization, from GPR time-slice analysis and three-dimensional ERT inversion modelling (Sapia et al. 2021), have considerably enhanced the interpretive resolution of the resulting datasets (Vergnano et al. 2025; Bornik and Neubauer 2022; Trinks and Hinterleitner 2020). The adoption of multi-sensor geophysical strategies offers significant advantages when facing the complexity of archaeological sites, often characterized by poorly preserved remains, complex pedology of subsoils and challenging topography (Comina et al. 2025; Zhao et al. 2015). Integrating complementary datasets from different methods reduces interpretive ambiguities, improves robustness and is especially valuable in contexts where overlapping structural phases occur (Wynn 1986; Monterroso-Checa et al. 2019; Porcelli et al. 2020; Russolillo et al. 2024). Nevertheless, each method carries specific sensitivities and limitations related to soil conditions, depth range and resolution trade-offs, which further underscores the value of such integrated approaches. The geophysical investigation of the *Palestra Grande* aimed at enhancing the reliability of subsurface archaeological prospection. The combined use of these techniques enabled the acquisition of complementary information on the geometry and physical properties of buried features, reducing uncertainties associated with individual methods. Survey design was tailored to the archaeological and environmental constraints of the site, allowing exploration from the near surface down to approximately 10 m of depth.

This study integrates UAV-based RGB and multispectral photogrammetry to support the metric documentation and archaeological interpretation of the Palestra Grande in Pompeii. High-resolution 3D models, orthophotos and spectral index maps were generated to analyse both exposed structures and potential buried remains. The adoption of direct photogrammetry with RTK positioning enabled centimetric accuracy while reducing field operations. Multispectral data and vegetation/soil indices (SIs) provided additional information beyond the visible range, highlighting possible anomalies linked to subsurface archaeological features. The complementary nature of these anomalies with respect to ground-penetrating radar (GPR) data is further exploited through a physically grounded integration analysis: Because buried archaeological features alter local soil moisture retention, which in turn influences surface vegetation vigour, a cross-correlation framework between NDVI-derived maps and GPR time-slice data is developed and applied to quantify the depth at which the two datasets decouple.

The presented multidisciplinary and multi-parametric results represent the first systematic geophysical assessment of the *Palestra Grande* and provide a crucial basis for refining hypotheses concerning the organization, extent and evolution of buried archaeological structures in this site of the Archaeological Park of Pompeii.

1.1 | Archaeological Framework

One notable architectural complex within the vast *Regio* II is the *Palestra Grande* (Pompei II 7) (Figure 2), situated near the amphitheatre (Parslow 2007 with earlier literature; Pesando and Guidobaldi 2006). It was built during the Augustan period, at the beginning of the 1st century AD and served as a

10990763, 0, Downloaded from https://onlinelibrary.wiley.com/doi/10.1002/arp.70066 by Valentina Santoro - Politecnico Di Torino Sist. Bibl Del Polit Di Torino , Wiley Online Library on [07/10/2026]. See the Terms and Conditions (https://onlinelibrary.wiley.com/terms-and-conditions) on Wiley Online Library for rules of use; OA articles are governed by the applicable Creative Commons License



FIGURE 2 | Overview of the area of *Regio II*, in red, its *insulae* and main roads. The *Palestra Grande* is highlighted in a yellow box, the amphitheatre in an orange circle.

vital hub for physical training and athletic activities in ancient Pompeii (Iadanza and Toniolo 2022; Maiuri 1939). The *Palestra Grande* was built in the Augustan period to complete an entertainment district established in the first century BC, after the foundation of the *Colonia Cornelia Veneria Pompeianorum*, when the nearby amphitheatre was constructed. It has been suggested that the construction of the *Palestra Grande* led to the dismantling of earlier buildings, probably domestic in nature (Ling 2007, 123). In any case, the establishment of this large complex brought about a series of significant changes in both public and private space. First, the connection between the area occupied by the amphitheatre and the *palestra* and the main carriage roads in this sector of Pompeii was reconsidered: running east–west towards Via di Nocera, the broad Via di Castricio was laid out, whereas running north–south towards Via dell'Abbondanza, Vicolo dell'Anfiteatro was widened (Iadanza and Toniolo 2022, 55). At the same time, the urbanization of the present-day *Insula* 4, corresponding to the *Praedia Iuliae Felicis*, was completed (Anguissola and Olivito 2022). This building was laid out as a large and diversified commercial complex, able to exploit—for *tabernae*, baths, fountains and the irrigation of the *hortus*—a hydraulic system that was already partly in existence and efficiently connected to the public network. In this period, the houses along Via di Nocera, whose original cores dated back at least two centuries, were renovated. Recent excavation work carried out in this sector, however, shows that these chronologies need to be refined and revised within the framework of an urban area that remained highly dynamic and active throughout the life of Pompeii (Anguissola and Olivito 2023; Anguissola and Olivito 2024; Anguissola and Olivito 2025). Understanding the building phases and history of the *Palestra Grande* is therefore essential for an accurate interpretation of the entire urban sector and, more broadly, of key aspects of the city's development, including the ways in which the relationship between public and private spaces and infrastructure was negotiated.

2 | Materials and Methods

2.1 | Geomatics Data Acquisition and Processing

The metric documentation of the *Palestra Grande* was obtained through a UAV-based photogrammetric survey employing both RGB and multispectral sensors. The investigation encompassed the *triporticus* and the central courtyard, extending over an area of approximately 15 400 m^2. Although the photogrammetric processing was carried out using the modern and efficient method of direct photogrammetry—as detailed in the following sections—it is important to note that the 3D surveying project was preceded by the establishment of a topographic network of vertices. This network was calculated both in the international reference system—now standard in cartography and Heritage documentation domain—and in the Great Pompeii reference system. This ensures that the results of past, current and future documentation efforts can be compared by individual researchers, as well as by research and administrative bodies—in this case the Archaeological Park of Pompeii—and all future stakeholders, following an approach already tested in comparable archaeological and Heritage documentation contexts (Porcelli et al. 2020). Further methodological details on the establishment of the topographic network are provided in Appendix S1.

10990763, 0, Downloaded from https://onlinelibrary.wiley.com/doi/10.1002/arp.70066 by Valentina Santoro - Politecnico Di Torino Sist. Bibl Del Polit Di Torino , Wiley Online Library on [07/10/2026]. See the Terms and Conditions (https://onlinelibrary.wiley.com/terms-and-conditions) on Wiley Online Library for rules of use; OA articles are governed by the applicable Creative Commons License

2.1.1 | RGB and Multispectral Photogrammetric UAV Survey

The data acquisition in the *Palestra Grande* pursued a dual objective: on the one hand, generating high-resolution 3D metric models with centimetric accuracy, correlated with previously excavated, exposed and restored structures; on the other, investigating buried remains and artefacts.

To accomplish these objectives, a UAV-based photogrammetric multi-sensor survey was carried out using the DJI Mavic 3M multispectral system (Table 1). This platform is equipped with a high-resolution RGB camera, along with four complementary metal oxide semiconductor (CMOS) sensors that enable the acquisition of multispectral images in specific ranges of the electromagnetic spectrum (green, red, red edge, near infrared [NIR] bands).

Traditionally, the integration of terrestrial survey methods with visible-spectrum aerial imagery applied to emerged structures requires a supporting topographic control network and the use of ground control points (GCPs). By contrast, the documentation of submerged structures enables the adoption of more expeditious techniques. In Pompeii, a direct photogrammetric approach was adopted for the 3D metric survey of the submerged structures of the *Palestra Grande*. This technique does not require the placement and measurement of GCPs on the site to scale and position the photogrammetric block. In fact, in direct photogrammetry, the coordinates of the centres of projections of the images are estimated during the acquisition through the navigation system embedded in the UAV (Chiabrando et al. 2013; Niu et al. 2024). In Pompeii, the DJI system employed was equipped with a real-time kinematic (RTK) module, used in combination with the network RTK service. This setup ensured accurate positioning data with centimetric accuracy, suitable for survey purposes.

TABLE 1 | Main specifications of DJI Mavic 3 multispectral cameras.

	DJI Mavic 3 multispectral	
UAV model	**RGB camera**	**Multispectral camera(s)**
Sensor(s)	4/3″ CMOS	Four 1/2.8″ CMOS
Effective pixels	20 [MP]	5 [MP]
Lens	Equivalent focal length: 24 mm Field of view: 84° Aperture: f/2.8–f/11	Equivalent focal length: 25 mm Field of view: 73.91° (61.2° × 48.10°) Aperture: f/2.0
Focal length	12.29 mm	4.34 mm
Sensor size	17.4 × 13 mm	5.2 × 3.9 mm
Image size	5280 × 3956	2592 × 1944
Wavelength (green)	—	560 nm ± 16 nm
Wavelength (red)	—	650 nm ± 16 nm
Wavelength (red edge)	—	730 nm ± 16 nm
Wavelength (near infrared)	—	860 nm ± 26 nm

The photogrammetric flight was planned at an altitude of 40 m to achieve a ground sampling distance (GSD) of approximately 1 cm per pixel for the RGB acquisition and 2 cm per pixel for the multispectral sensors, enabling a very detailed description of the courtyard of the *Palestra*. The difference between the two GSD values arises from the fact that, in general, the geometric resolution of multispectral sensors is lower than that of traditional ones operating in the visible range of the electromagnetic spectrum. A total of 600 images were acquired, of which the RGB camera captured 120, whereas the other 480 were acquired by the multispectral sensors, with overlaps among images and stripes fixed at 70%. The multispectral images were subsequently subjected to radiometric calibration during photogrammetric processing in Agisoft Metashape. In the present survey, no ground-based reflectance calibration panel was used. Instead, the *Calibrate Reflectance* procedure was applied using the measurements recorded during acquisition by the sunlight sensor integrated into the UAV. According to the Metashape processing workflow, the sun-sensor measurements are used to account for variations in incident illumination and to calibrate the reflectance factors of the multispectral bands. The calibrated multispectral data were retained in their 16-bit representation and directly used for the calculation of normalized spectral indices. For non-normalized spectral indices, the calibrated 16-bit band values were first converted to dimensionless reflectance factors by dividing the pixel values by 32 768, according to the scaling convention indicated by Agisoft Metashape Technical Support, whereby a value of 32 768 corresponds to 100% reflectance (Agisoft LLC 2025). At the end of the photogrammetric process and orientation of both RGB and multispectral images, the accuracy of the estimation of the coordinates of the camera centres resulted in a root mean square error (RMSE) of 0.019 m for the RGB images and 0.041 m for the multispectral sensors; these values were consistent with the scale of the survey and the planned GSD.

The photogrammetric acquisition yielded three primary outputs: two point clouds, a DSM and two orthophotos (Tables 1 and 2). Specifically, the RGB acquisition produced a point cloud/model, an RGB orthophoto and a DSM of the site (Table 2), fundamental in providing an accurate and high-resolution 3D mapping of the site and its exposed structures. These value-added metric products have been useful in obtaining a model of the *Palestra*, in the analysis of spatial connections between different areas of the urban archaeological park and the characterization of the courtyard terrain. The latter has been used as a ground truth for the following comparison with the multispectral acquired data.

Simultaneously, the multispectral cameras enabled the generation of a multispectral and multiband orthophoto (Table 3), which provided information not observable in the visible range of the electromagnetic spectrum. This additional data could be associated with buried structures and artefacts, aligning with one of the main primary objectives of the survey.

10990763, 0, Downloaded from https://onlinelibrary.wiley.com/doi/10.1002/arp.70066 by Valentina Santoro - Politecnico Di Torino Sist. Bibl Del Polit Di Torino , Wiley Online Library on [07/10/2026]. See the Terms and Conditions (https://onlinelibrary.wiley.com/terms-and-conditions) on Wiley Online Library for rules of use; OA articles are governed by the applicable Creative Commons License

TABLE 2 | Main features of the added-value metric products from acquisition.

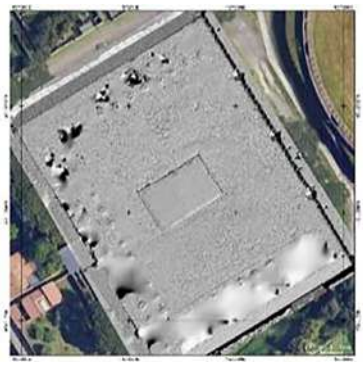
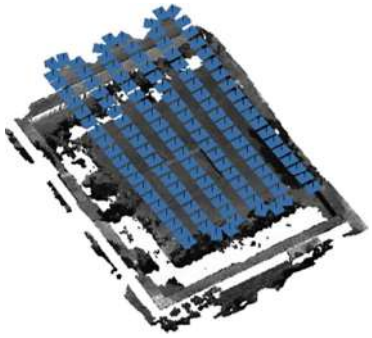
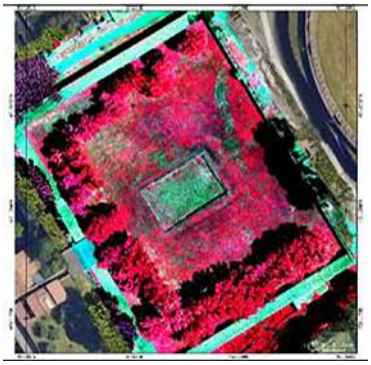
RGB dataset				
Point cloud	**DSM**		**Orthophoto**	
Density [points/m²]	**Resolution [cm/pixel]**	**Dimensions [pixel]**	**Resolution [cm/pixel]**	**Dimensions [pixel]**
1220	2.2	7644 × 8498	1	16 950 × 18 844
				

TABLE 3 | Main features of the added-value metric products from multispectral acquisition.

Multispectral dataset		
Point cloud	**Orthophoto**	
Density [points/m²]	**Resolution [cm/pixel]**	**Dimensions [pixel]**
660	1	16 948 × 18 842
		

2.1.2 | Multispectral Index Maps

Based on the multispectral and RGB orthophotos, an extended analysis of the *Palestra Grande* courtyard has been carried out (maps and spectral indices descriptions are in Appendix S2). It aimed to detect anomalies that could be connected to the presence of buried artefacts and structures, affecting the spectral response of both soil and vegetation of the yard. The initial analysis was conducted through visual photointerpretation, through spectral indices calculation, a well-established approach used to improve data readability. Six different index maps were calculated in QGIS, taking advantage of specific tools for band management and representation.

Considering the condition of the vegetation existing in the court of the *Palestra Grande*, which was mowed just before the photogrammetric acquisition, four vegetation indices (VIs) have been calculated. In general, they allow assessing vegetation health, foliage, cover or phenology (Glenn et al. 2008) and, consequently, the response to buried structures that may affect its growth.

The normalized difference vegetation index (NDVI) represents one of the most-used indices in RS applications since its first formulation in 1973 for vegetation monitoring (Rouse et al. 1974) and, later, also to assess buried archaeological sites (Agapiou and Hadjimitsis 2011). It considers the reflected energy in the red band—absorbed by the chlorophyll—and the one reflected in the NIR, connected to the leaves' scattering. It provides a useful indicator of the health and greenness of vegetation (Fraser and Congalton 2021). The normalized difference red edge (NDRE), instead, apart from the NIR

10990753, 0, Downloaded from https://onlinelibrary.wiley.com/doi/10.1002/arp.70066 by Valentina Santoro - Politecnico Di Torino Sist. Bibl Del Polit Di Torino , Wiley Online Library on [07/10/2026]. See the Terms and Conditions (https://onlinelibrary.wiley.com/terms-and-conditions) on Wiley Online Library for rules of use; OA articles are governed by the applicable Creative Commons License

contribution, also considers the red edge (RE) band of the spectrum, in which lies the rapid change in reflected energy of vegetation. This index has been particularly useful in detecting forest health issues (Yu et al. 2022) and also in detecting early symptoms of stress and infested vegetation, responding to low chlorophyll levels (Marx et al. 2024). The Enhanced Vegetation Index—2 (EVI 2) is a modified version of the Enhanced Vegetation Index (EVI), in which the contribution of the blue spectral band is excluded. It is commonly employed in the calculation to reduce noise and account for atmospheric aerosol variability (Jiang et al. 2008). In this context, EVI 2 enables a comparable computation of EVI, but without requiring the blue band, making it particularly suitable in cases where sensors not acquiring this specific band are exploited. EVI 2 also shares similarities with NDVI, as both rely, in their calculation, on NIR and red spectral bands. However, unlike NDVI, EVI 2 considers the contribution of environmental factors such as soil background or atmospheric condition, enabling improved vegetation monitoring (Matsushita et al. 2007).

To account for the presence of bare soil and sparsely vegetated surfaces in the *Palestra* court, the application of SIs was considered valuable. The brightness index (BI) is useful for assessing the condition of the bare soil within the court area, particularly in light of the vegetation having been mown shortly before data acquisition, thereby exposing extensive soil surfaces. Indeed, as demonstrated in a previous research study (Salgado Carmona et al. 2020), this index produced promising results in the detection of archaeological remains in Mediterranean-type landscapes—such as Pompeii—characterized by irregular rainfall reflecting on soil characteristics variations. Moving from the contribution of the BI and considering the drought phenomena interspersed with episodes of heavy rains that affected Pompeii in the weeks preceding data acquisition (Centro Funzionale Multirischi di Protezione Civile Regione Campania 2023), the calculation of the normalized difference water index (NDWI) was also performed. Although it is primarily employed in hydrology for mapping water areas, hydric features and groundwater elements (Rana et al. 2025), the NDWI is also used to assess vegetation and soil humidity content (Dragomir et al. 2012), which motivated its application in the context of Pompeii. Lastly, the singular contribution of the NIR spectral band has been considered through the RN (red + NIR) index, already positively explored in previous archaeological research (Zanni and De Rosa 2019). It is a combination of the red and NIR bands, leveraging the spectral characteristics of vegetation in these wavelengths.

2.1.3 | Data Analysis

A detailed analysis was conducted based on the calculation of the spectral index maps, which represent a well-established approach in visual photointerpretation, and their comparison with the RGB orthophoto. It aimed to identify elements, colour contrasts and anomalies in the maps that may, e.g., considering VIs, indicate stressed vegetation or alterations in growth. Specifically, the visual analyses considered two elements of the surveyed surfaces and structures:

- Radiometric features, based on local variations and contrasts in spectral-index values;
- Geometric elements, including shape, size, patterns and shadows.

The radiometric analysis focused on local variations and contrasts in spectral-index values, which may reflect spatial variations in vegetation or soil conditions. Anomalies were identified as spatially localized contrasts in index values relative to the surrounding background under comparable land-cover conditions. In vegetated areas, particular attention was given to spectral anomalies associated with variations in vegetation growth and vigour, as these may be indicative of archaeological crop marks (Agapiou and Hadjimitsis 2011; Agapiou et al. 2013). Specifically, the analysis focused on the low-grass-covered areas of the Palestra Grande courtyard, whereas tree-covered areas were not considered for anomaly detection. The anomalies were highlighted by adjusting the visualization range of each spectral-index map through histogram stretching, thereby supporting their visual identification and analysis.

The geometric input, instead, focused on the geometry of the anomalies, also enabling the definition of contours and shadows. Shadows require careful consideration due to their influence on the spectral response. Because shadows typically produce low or negligible spectral response, they can generate areas of contrast within the frame, which may lead to interpretive deviations (Adler-Golden et al. 2002; Pons and Padró 2021). To mitigate such misinterpretations and address the influence of artificial elements existing in the surveyed areas, the spectral indexes maps were cross-referenced and compared with the RGB orthophoto of the *Palestra Grande*.

Based on these considerations, the detection and interpretation of anomalies were guided by two main criteria. Firstly, it is noteworthy that some anomalies were already detectable in the RGB orthophoto, e.g., as areas characterized by paler-green vegetation. For this reason, they were analysed separately from those detected exclusively through the analysis of spectral indices. Secondly, the anomalies detection prioritized pseudo-geometric, regular or well-defined shapes, such as rectangles, regular polygons or circular features (Moriarty et al. 2019). The described visual analyses were carried out through QGIS (v. 3.34.13), which also allowed the geolocated comparison and integration of heterogeneous datasets within a single working environment, enabling their cross-correlation analysis.

2.2 | Geophysical Data Acquisition and Processing

The geophysical investigation of the area was performed through GPR and ERT. Three GPR grids were acquired following the U-shaped geometry displayed in Figure 3, surrounding the pool at the centre of the garden. It was not possible to investigate the missing transect due to logistical impediments, as well as the presence of tall trees that obstructed GNSS signal reception. The two ERT profiles A and B (Figure 3) were collected respectively in the northern and southern areas of the garden. With this approach, we were able to obtain detailed subsurface information from the near surface, up to a depth of about 10 m. Recovered models from each geophysical prospecting technique provided a complex subsurface layout, characterized by clear anomalies

10990763, 0, Downloaded from https://onlinelibrary.wiley.com/doi/10.1002/arp.70066 by Valentina Santoro - Politecnico Di Torino Sist. Bibl Del Polit Di Torino , Wiley Online Library on [07/10/2026]. See the Terms and Conditions (https://onlinelibrary.wiley.com/terms-and-conditions) on Wiley Online Library for rules of use; OA articles are governed by the applicable Creative Commons License

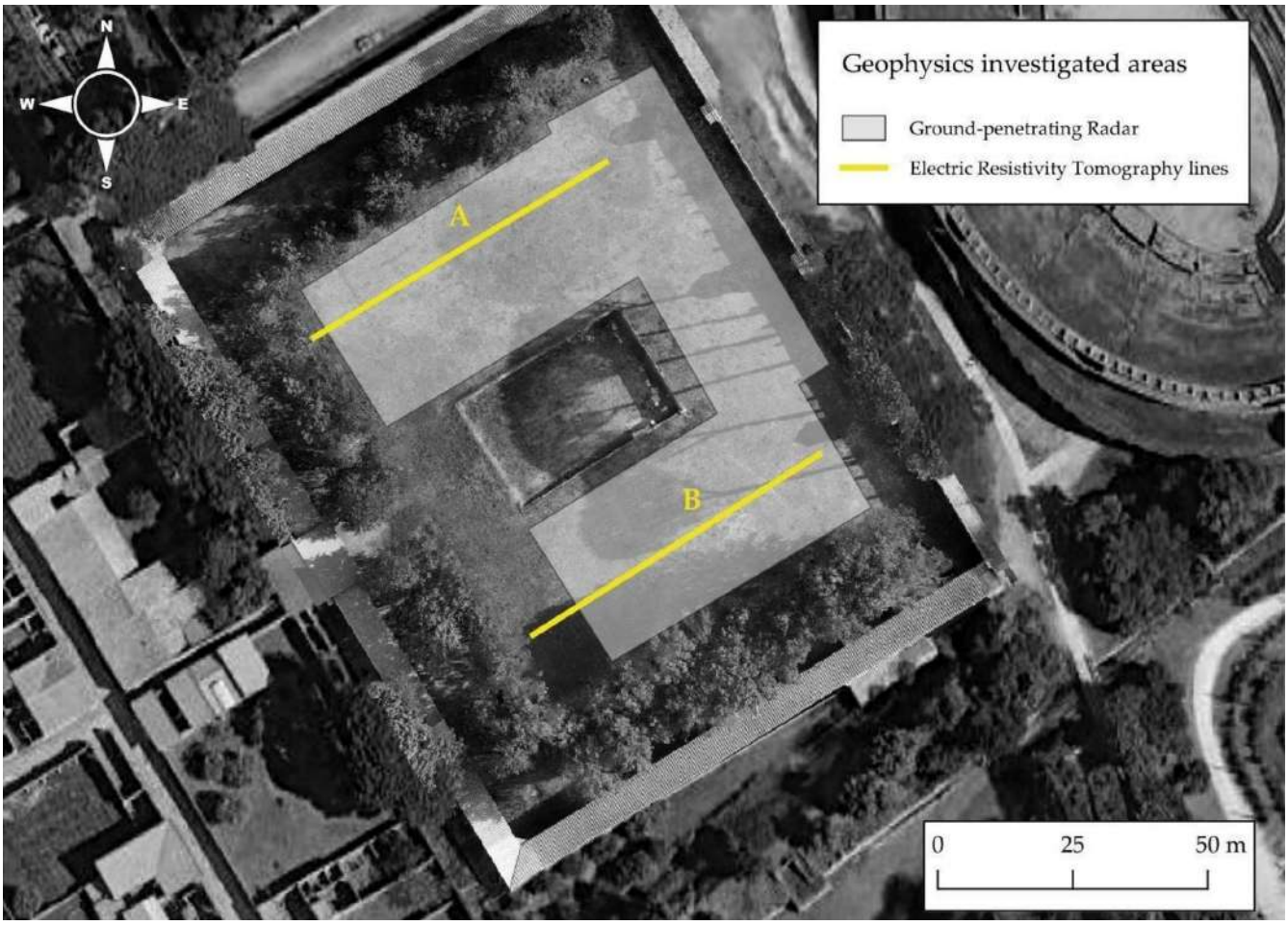


FIGURE 3 | The locations of geophysical surveys conducted in the *Palestra Grande*. ERT profiles A and B are marked with yellow lines, whereas the grids investigated by GPR are indicated by a white U-shaped polygon.

of different nature and geometry. In the following paragraphs the methodologies, acquisition techniques and data processing workflow are presented.

2.2.1 | Electric Resistivity Tomography (ERT)

Two 64 m long ERT profiles were acquired in *Palestra Grande* (Figure 3) with electrode spacing of 1 m; the positions of the electrodes were measured through differential Global Navigation Satellite System (GNSS). The array was designed to reach an approximate depth of investigation of 10 m while still maintaining an acceptable resolution in the shallow subsurface because potential archaeological targets were expected in the first 2 m b.g.l.

Before acquisition, contact resistance checks were used to avoid high resistance readings, and fresh water was poured into the ground to improve electrode coupling. Data acquisition was managed through a Syscal R2 (IRIS Instruments) georesistivimeter, which injected 250 ms square waves with a voltage of 100 V into the ground. For each profile, we employed both dipole–dipole (DD) and Wenner–Schlumberger (WS) sequences to combine vertical and horizontal resolution (Loke and Barker 1995). Data filtering was aimed to exclude significant outliers and very low voltage/current readings.

The inversion of ERT data was performed using the smoothness-constrained least-squares (Occam-style) algorithm implemented in ResiPy (Blanchy et al. 2020). The software implements an 'Occam-style' inversion approach (Binley and Kemna 2005; Constable et al. 1987) that minimizes a regularized objective function (L2-norm) to combine a data misfit term, based on a least squares formulation, with a model smoothness constraint. With this approach, the subsurface is initially represented by a homogeneous half-space model, and the resistivity distribution is iteratively updated by minimizing an objective function that combines the data misfit with a model roughness constraint. Meshing was handled through Gmesh, a complementary mesh generator for ResiPy (Geuzaine and Remacle 2009). A triangular elements mesh was generated with the following parameters: (i) growing factor = 2; (ii) characteristic length = 0.25 m, which is equal to ¼ of electrode spacing; (iii) growth rate = 5 m (depth at which mesh polygons are double the size of superficial ones). To initialise the inversion, we used the average value of the apparent resistivity data distribution as starting model of the inversion. The software allows different options to address the starting model of the inversion, but we used the default approach that assigns a uniform resistivity which is estimated from the apparent resistivity data. For our two profiles, we used the average of the measured apparent resistivities which was around 250 Ωm. After, respectively, six and seven iterations, Models A and B converged to an RMSE of 1.10 and 1.19.

10990763, 0, Downloaded from https://onlinelibrary.wiley.com/doi/10.1002/arp.70066 by Valentina Santoro - Politecnico Di Torino Sist. Bibl Del Polit Di Torino , Wiley Online Library on [07/10/2026]. See the Terms and Conditions (https://onlinelibrary.wiley.com/terms-and-conditions) on Wiley Online Library for rules of use; OA articles are governed by the applicable Creative Commons License

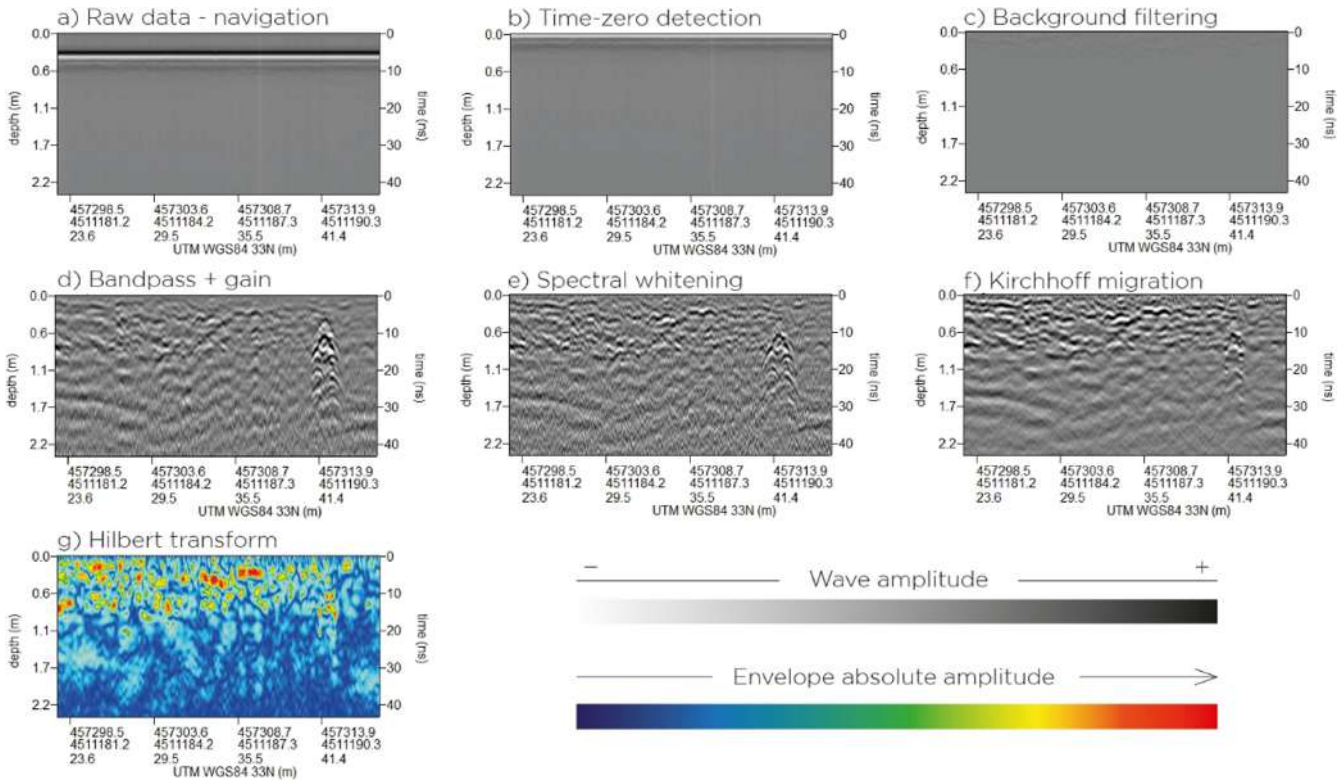


FIGURE 4 | Progressive steps of GPR data filtering on a representative B-scan.

2.2.2 | GPR

The grey area displayed in Figure 3 was investigated through a Stream-X (IDS Georadar) multichannel GPR array, consisting of seven 200 MHz VV dipoles with a spacing of 12 cm. The instrument is mounted on a custom cart and interfaced with a differential GNSS receiver. GPR signal is synchronized with GNSS timestamps through pulse per second (PPS) connection, whereas the trigger of electromagnetic pulses is managed by a magnetic encoder installed on the front-left wheel of the cart. Data collection was handled through the software OneVision (IDS Georadar) to set acquisition parameters which include a time window of 90 ns, 512 samples/scan and in-line trace spacing of 0.045 m. GPR profiles were acquired in parallel lines and positioning was managed through real-time navigation in OneVision, yielding a regular spatial sampling of 0.12 × 0.045 m.

We processed GPR data with GPR-Slice software (Screening Eagle Technologies) (Figure 4). After assigning markers for the correct positioning of the original radar scans (a) we applied the following filtering algorithms (Goodman 2008) to enhance GPR signal: (b) Static correction through automatic thresholding (0.5 amplitude of the first positive peak), (c) Background noise removal (full-trace), (d) Band-pass filtering (135–700 MHz) and application of an automatic gain curve (AGC), (e) Spectral whitening to equalize the spectral content of scans and recover high-frequency detail at depth, (f) Kirchhoff migration and determination of the velocity model of the medium through hyperbola fitting, (g) Hilbert transform, to extract the envelope and instantaneous phase of the signal.

Through hyperbola fitting, we calculated an averaged ground radar-wave velocity of 0.112 m/ns, which results in an estimated depth of investigation of about 2 m (about 230 ns), below which signal/noise ratio drops significantly. Two 3D pulse volumes were generated from Hilbert-transformed and migrated radargrams; the first volume expresses the absolute amplitude of reflections, whereas the second one retains both intensity and polarity of the reflections. From these volumes two sets of maps were sliced at 2 cm depth increments to map the distribution of dielectric anomalies in the subsurface (the complete set of time-slices is available in Supporting Information).

3 | Results and Discussion

This study specifically focuses on supporting archaeological interpretation and the assessment of non-excavated structures within the study area. A key contribution of this study lies in the systematic comparison and integration of geomatics and geophysical results. The visual interpretations derived from the spectral indices and the geophysical results were assessed and compared with enable a comprehensive evaluation of the different methods and to maximize the complementary value of photogrammetric and geophysical datasets. Both qualitative visual inspection and quantitative analysis were performed. This work introduces a semi-automatic cross-correlation analysis to improve the efficiency of data comparison, traditionally reliant on time-consuming manual procedures. The method enables the systematic integration and cross-analysis of spectral index maps (such as NDVI) and GPR time-slices, enhancing the complementary exploitation of both datasets.

10990763, 0, Downloaded from https://onlinelibrary.wiley.com/doi/10.1002/arp.70066 by Valentina Santoro - Politecnico Di Torino Sist. Bibl Del Polit Di Torino , Wiley Online Library on [07/10/2026]. See the Terms and Conditions (https://onlinelibrary.wiley.com/terms-and-conditions) on Wiley Online Library for rules of use; OA articles are governed by the applicable Creative Commons License

3.1 | Geomatics

The visual analysis performed for each cited index has proven to be particularly effective, resulting in a series of anomalies distributed around the central *natatio* of the *Palestra Grande* (Figure 5). As relevant examples, several anomalies are aligned with the longitudinal orientation of the *Palestra*, extending towards the *natatio* (a) whereas another large circular (b, approximately 9 m radius) anomaly is located adjacent to the *Palestra* wall towards the amphitheatre, on the south-east side of the yard (zoom-in views of the anomalies are presented in Appendix S3).

From a preliminary investigation, moving from the different purposes and sensitivities of the used spectral indices, the anomalies were not always detected by all six employed indices. For this reason and with the aim of understanding which spectral index performed better in these conditions and also which spectral band is more relevant and useful in the detection, each anomaly has been classified considering how many times it has been detected in the different indices (confidence). This value was considered as a qualitative indication of the consistency and recurrence of anomaly detection across the different spectral-index maps. The range of values is expressed between 1 and 6, where 1 means that the anomaly has been detected in only one index map, without any other recall, whereas 6 means that the anomaly has been detected in all the index maps (Figure 6). Only two anomalies were detected in a single index map, in both cases RN, whereas four anomalies were detected multiple times in all the indices maps. Specifically, PG3 and PG2 (Figure 6) show very similar, regular and rectangular shapes, aligned with the longitudinal orientation of the *Palestra* and heading to the centre of the *natatio*, almost defining an axis of the courtyard. PL4 and PL5, instead, align on a circular shape. These four anomalies represent examples of negative crop marks, characterized by a reduced vegetation growth that can be related to buried artificial (like walls or roads) structures that negatively affected the water and nutrients supply of the plants (Gojda and Hejcman 2012). PL8, instead, which was detected in only one index map, represents a positive crop mark, characterized by a darker green and healthier foliage, that can be connected to buried material that retains dampness and nutrients for the vegetation (Agapiou et al. 2013).

Based on the count of detected anomalies (Figure 7), NDVI, NDWI, EVI2 and BI are the most effective indices, followed by the combination of red and NIR bands; lastly, NDRE. The number of anomalies detected in each index map was considered as a descriptive criterion to compare their response under the specific conditions of the present survey, as similar comparisons based on the number of identified archaeological features have been adopted in previous archaeological remote-sensing studies (Bennett et al. 2012). The calculation of the number of detected anomalies does not take into account their dimensions or extensions.

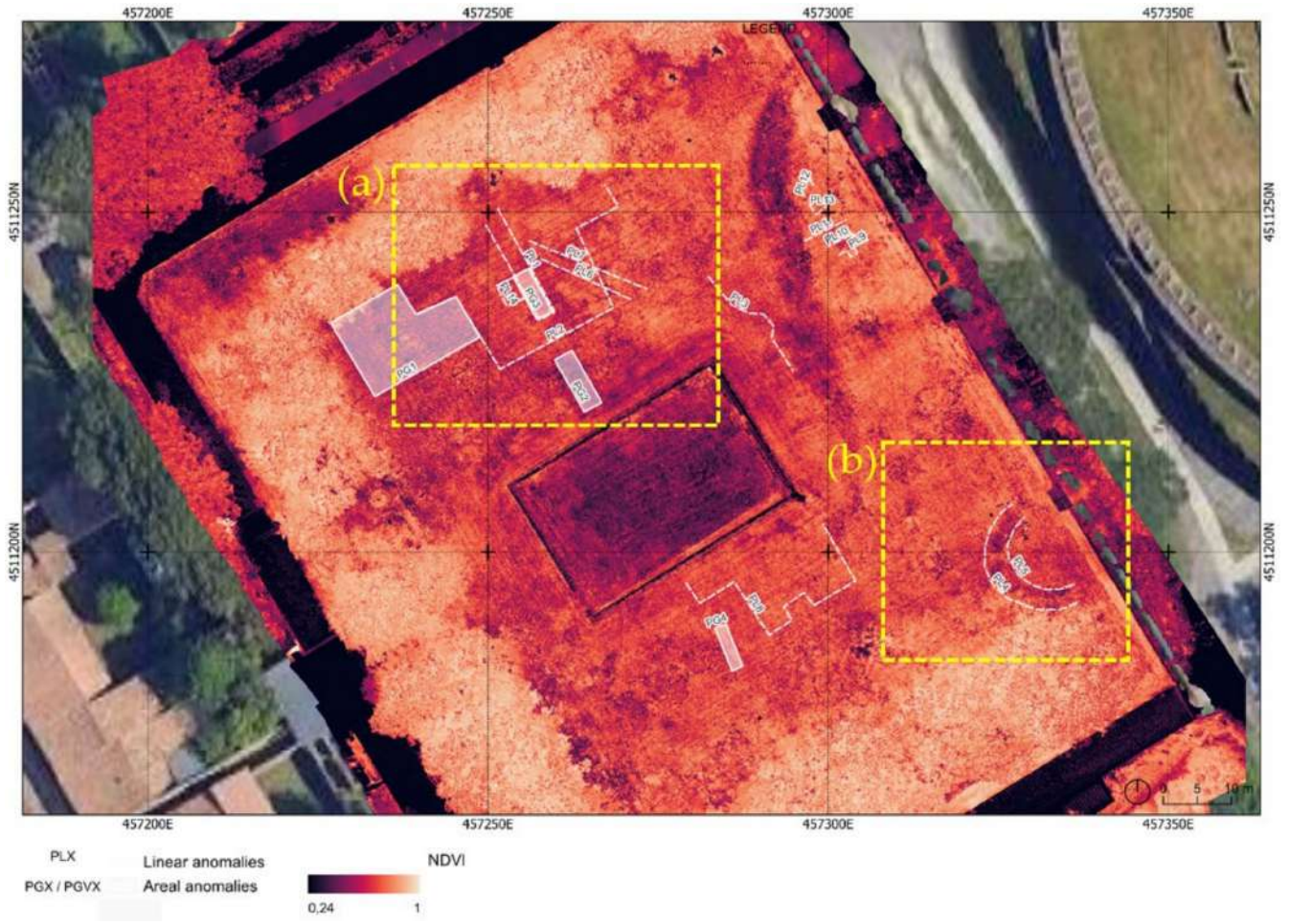


FIGURE 5 | Detected spectral anomalies—in white—overlapped on the normalized difference vegetation index map. Yellow rectangles (a), (b) indicate areas corresponding to zoomed-in images of specific anomalies.

10990763, 0, Downloaded from https://onlinelibrary.wiley.com/doi/10.1002/arp.70066 by Valentina Santoro - Politecnico Di Torino Sist. Bibl Del Polit Di Torino , Wiley Online Library on [07/10/2026]. See the Terms and Conditions (https://onlinelibrary.wiley.com/terms-and-conditions) on Wiley Online Library for rules of use; OA articles are governed by the applicable Creative Commons License



FIGURE 6 | Map of anomalies detected by spectral index analyses. The colour of each anomaly represents its qualitative 'confidence', i.e., the number of spectral index maps in which it was detected.

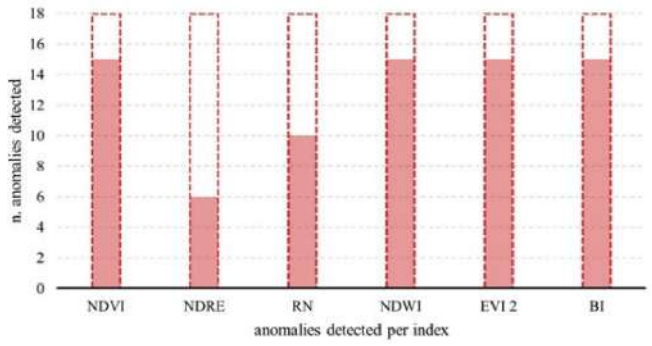


FIGURE 7 | Comparison of the six spectral indices based on the total number of anomalies detected in each index map.

Regarding NDRE, it has been especially useful in detecting forest health issues (Yu et al. 2022) and also in detecting early symptoms of stress and infested vegetation, responding to low chlorophyll levels (Marx et al. 2024). However, considering the condition of the vegetation in the *Palestra Grande* and also its growth, it did not help in the detection of anomalies, although under specific circumstances and stretched values, it confirmed already detected areas.

Regarding the bands involved in the index calculation, under the conditions of the present survey, indices incorporating the NIR band generally highlighted more anomalies than those relying on the RE band. RE is particularly responsive to physiological changes in vegetation, such as chlorophyll content or leaf maturity and is connected to the pigment variation content in the single leaves. In contrast, the NIR band is associated with the internal cellular structure and its degradation, responsive to water content and nutrient deficit (Verhoeven and Doneus 2011). These spectral responses are closely linked to the specific phenological stages of the vegetation (Agapiou et al. 2013; Zhang et al. 2025) and its vigour. Consequently, a more comprehensive comparison of the spectral indices would require multitemporal UAV acquisitions, allowing different stages of vegetation growth to be considered and their response to buried archaeological features to be assessed.

In addition to the anomalies detected through spectral-index analysis, further irregular anomalies were observed in the RGB orthophoto, particularly in areas where vegetation appeared fainter (Figure 8). These were also clearly highlighted in the index maps. Their visibility in the RGB orthophoto indicates that the reduced vegetation vigour was perceptible even without spectral enhancement (zoom-in views are presented in Appendix S4).

10990763, 0, Downloaded from https://onlinelibrary.wiley.com/doi/10.1002/arp.70066 by Valentina Santoro - Politecnico Di Torino Sist. Bibl Del Polit Di Torino , Wiley Online Library on [07/10/2026]. See the Terms and Conditions (https://onlinelibrary.wiley.com/terms-and-conditions) on Wiley Online Library for rules of use; OA articles are governed by the applicable Creative Commons License



FIGURE 8 | Totality of anomalies detected in *Palestra Grande*. The ones in purple are detected in the RGB orthophoto. Red squares (a), (b) indicate areas corresponding to zoomed-in images of specific anomalies, highlighting vegetation anomalies already detectable in the RGB orthophoto.

Some limitations should also be acknowledged. The recent grass-cutting left visible mower tracks, affecting the photogrammetric UAV-acquired data and their subsequent analysis. These marks remained visible in the spectral-index maps, making their interpretation more difficult. The mechanical impact of the lawnmower wheels visibly altered the vegetation, potentially generating local contrasts in the spectral-index maps and leading to their misinterpretation. Additionally, the presence of dense tree canopies influenced both data acquisition (including flight height) and subsequent analysis, restricting the availability of unobstructed areas. The trees also cast extensive shadows across the *Palestra Grande*, further influencing the spectral response of the underlying vegetation and, consequently, its interpretation.

3.2 | Geophysics

3.2.1 | ERT Results

The ERT results are presented in Figure 9. The sections show the 2D distribution of electrical resistivity up to a depth of approximately 10 m below ground level.

Both profiles reveal a layered electro-stratigraphic structure: a shallow and superficial layer of variable thickness, with resistivity values around 400–600 Ωm; an intermediate layer is found below, with lower resistivity values (approximately 50–200 Ωm) and an average thickness of about 4 m; because the current surface of Pompei corresponds to the pre-79 AD Roman paleosol, this conductive layer likely corresponds to protohistoric volcanoclastic deposits, which were recognized and observed at comparable depths in previous studies (Vogel and Märker 2011, 2012). The deepest recognizable layer extends to the bottom of the model and exhibits higher resistivity values, which locally exceed 1000 Ωm. The discontinuity between conductive and resistive layers is found at variable depths in both profiles, ranging from 5 to 8 m b.g.l.

Notably, ERT profile A presents a superficial high-resistivity anomaly which extends approximately 12 m and reaches a thickness of about 1 m. Moreover, clear discontinuities are visible in the conductive layer. The general behaviour of ERT profiles marks the presence of a shallow discontinuity between the exposed Roman paleosol and antecedent volcanic deposits. Deeper, a large lens-shaped resistive anomaly is found in both sections, likely corresponding to dry coarse volcanic deposits, as already recognized in Vogel and Märker (2012).

10990763, 0, Downloaded from https://onlinelibrary.wiley.com/doi/10.1002/arp.70066 by Valentina Santoro - Politecnico Di Torino Sist. Bibl Del Polit Di Torino , Wiley Online Library on [07/10/2026]. See the Terms and Conditions (https://onlinelibrary.wiley.com/terms-and-conditions) on Wiley Online Library for rules of use; OA articles are governed by the applicable Creative Commons License

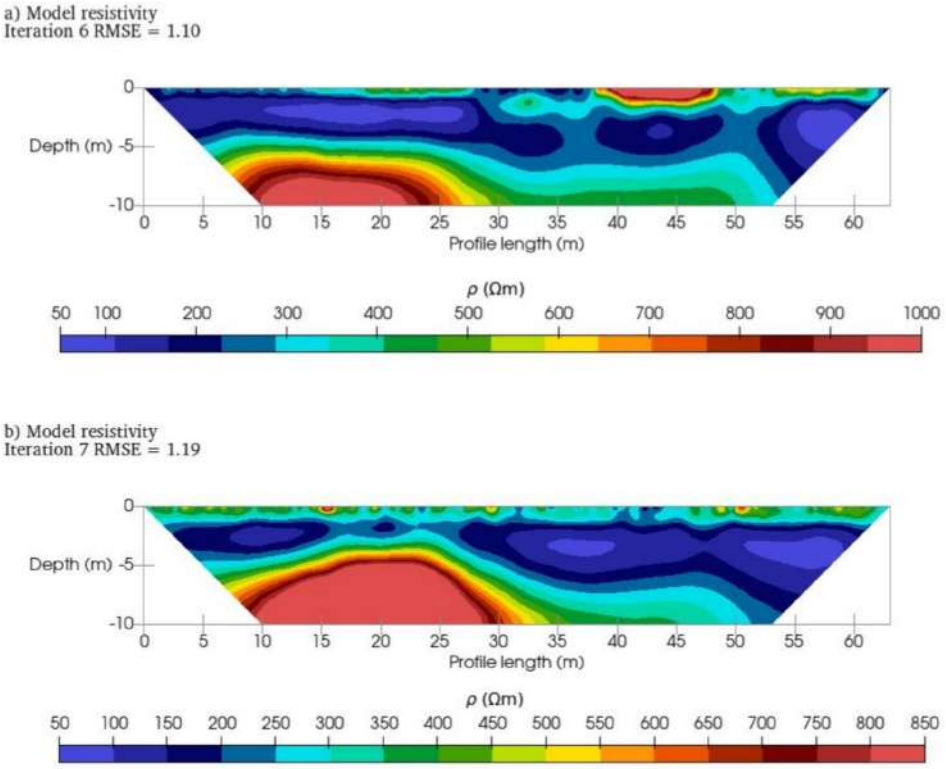


FIGURE 9 | ERT profiles inverted through Resipy. The upper panel displays Section A, whereas Section B is in the lower panel. Resistivity values range from 50 to 1000 Ωm in Section A and from 50 to 850 Ωm in Section B. High resistivity values are displayed in red, whereas conductive materials are shown in blue.

3.2.2 | GPR Results

Through filtering procedures and data interpolation, GPR data are especially clear in the uppermost 1.5 m of subsurface: No evident instrumental artefacts are present, and high signal/noise ratio allows to easily recognize dielectric anomalies. Below 1.5 m reflections are still distinguishable, but a notable striping effect starts to hamper the quality of results; this is likely due to the electromagnetic signal reaching a more conductive layer of the subsurface. The set of time-slices displayed in the following Figure 10 shows the weighted sum of the dielectric response within 0.25 m thick slices of the envelope GPR volume, from the surface to 2.0 m b.g.l.

The complete overview of dielectric subsurface features yields a rather complex ensemble of shapes, ranging from linear to rounded to chaotic reflectors. Strong linear anomalies appear at varying depths; they all seem to be functionally linked to the *natatio* at the centre of the courtyard. A shallow (0.00–0.50 m b.g.l., Panels a and b of Figure 10) and very energetic linear anomaly can be found in the eastern sector: its reflection (an isolated and energetic diffraction hyperbola) suggests this object may be a metallic or PVC pipe. Another linear anomaly can be found in the north-west side of the yard, close to a rounded geometry and to a corner of the pool. Two more linear reflectors are located in the southern sector: the first is found at depths between 0.50 and 2.00 m b.g.l.; when observed in section it seems to delineate a slightly arched profile at the top. The second emerges at 2.00 m b.g.l., and as for the previous one, it connects with the south-east edge of the pool. The reflection of this object is quite different from the previous one, as once migrated, it appears as a dot. Furthermore, it appears quite slimmer in the top view than the one next to it; however, this effect may be due to the greater depth at which the reflection is found and its conductive surroundings.

Additionally, patterns of dielectric anomalies emerge at various depths, displaying various shapes which are challenging to interpret. The first one appears as a dotted arched pattern, which emerges in the very first layers of the subsurface (0.25–0.75 m b.g.l., Panels b and c of Figure 10). The second one is a set of elongated reflections, between 0.50 and 0.75 m b.g.l., under the treeline in the western sector of the maps. The proximity to the trees may suggest these objects are tree roots.

To examine the most significant reflections, a joint analysis of time-slice and B-scan sections was performed: Some notable anomalies are highlighted in Figure 11, and their reflections are reported in B-scan profiles of Figure 12. The map of Figure 11 is extracted from the Kirchoff migration volume at 0.53 m b.g.l.: We found that incorporating polarity of the reflection along with its amplitude can display changes in textural behaviour of the subsurface more clearly.

Although some notable reflections do not appear in the selected sections (D and E in Figure 11), their shapes and location in proximity of the *natatio* suggest they may be functionally linked to its functioning, as linear and rounded anomalies could be due respectively to piping and cisterns. At the same time, some reflections which do not appear in the map of Figure 11 can be

10990763, 0, Downloaded from https://onlinelibrary.wiley.com/doi/10.1002/arp.70066 by Valentina Santoro - Politecnico Di Torino Sist. Bibl Del Polit Di Torino , Wiley Online Library on [07/10/2026]. See the Terms and Conditions (https://onlinelibrary.wiley.com/terms-and-conditions) on Wiley Online Library for rules of use; OA articles are governed by the applicable Creative Commons License

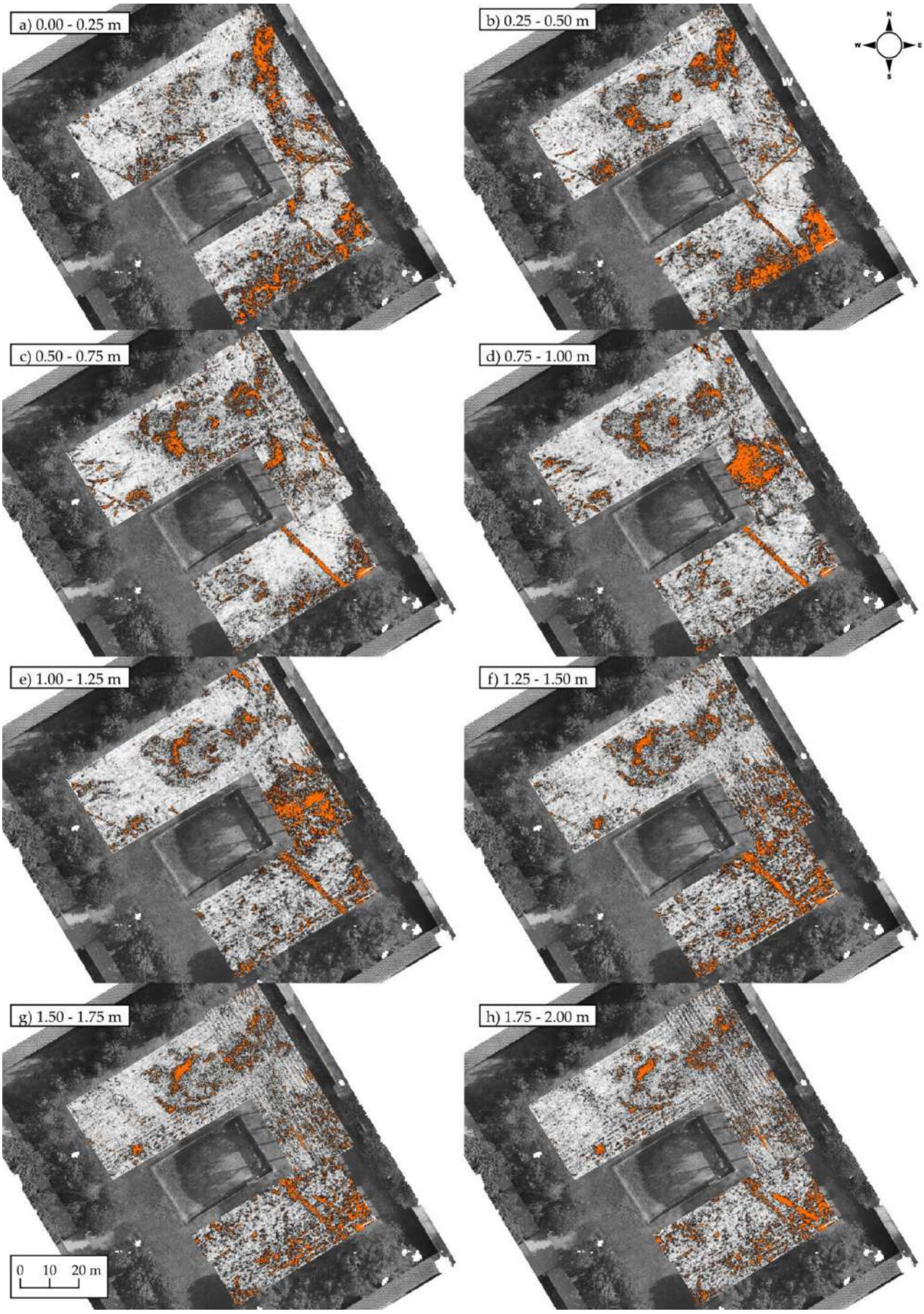


FIGURE 10 | Legend on next page.

10990753, 0, Downloaded from https://onlinelibrary.wiley.com/doi/10.1002/arp.70066 by Valentina Santoro - Politecnico Di Torino Sist. Bibl Del Polit Di Torino , Wiley Online Library on [07/10/2026]. See the Terms and Conditions (https://onlinelibrary.wiley.com/terms-and-conditions) on Wiley Online Library for rules of use; OA articles are governed by the applicable Creative Commons License

FIGURE 10 | A comprehensive view of the subsurface dielectric anomalies through GPR time slices. Each map is the result of the weighted sum of 25 cm intervals of the Hilbert pulse volume.

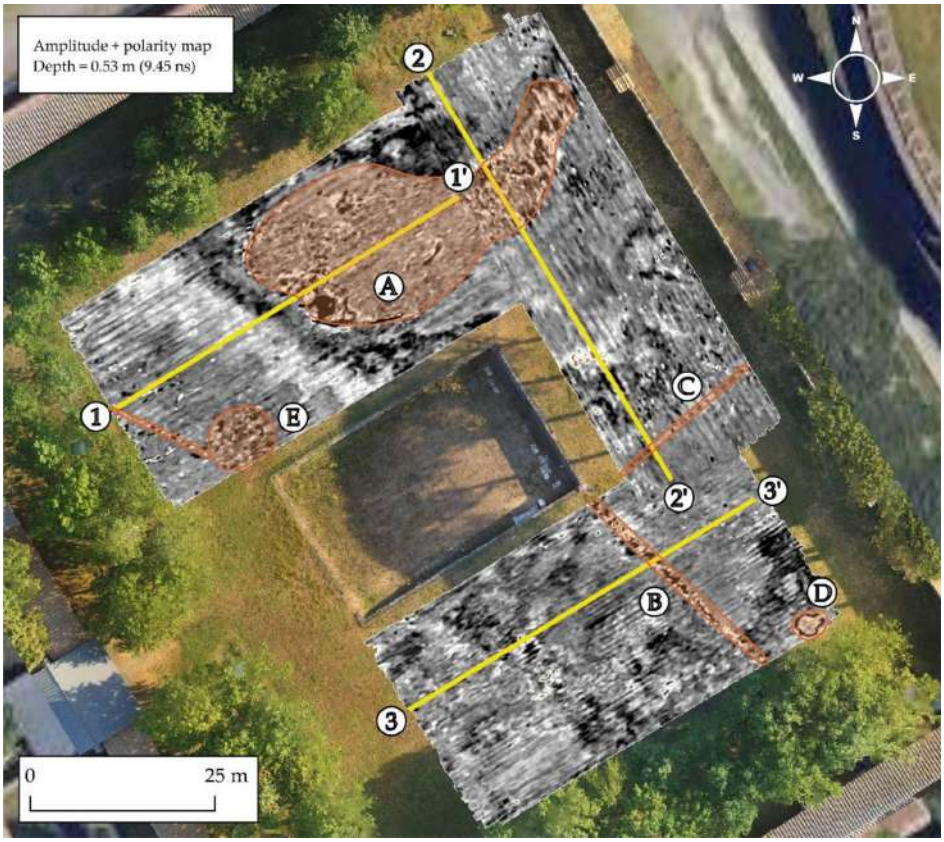


FIGURE 11 | Kirchoff migration time-slice at 0.53 m b.g.l. (9.45 ns corrected return time). Notable anomalies are highlighted in orange, whereas B-scan sections 1–1′, 2–2′ and 3–3′ are marked in yellow.

observed in section view: most notably, a deep diffractor next to reflection B in profile 3–3′ which was recognized as a deep linear anomaly and a strong continuous interface in profile 1–1′.

We cannot exclude that some rounded anomalies may represent explosion craters, as the area was severely affected by the aerial bombardments that struck Pompeii between August and September 1943. Recent research has further elucidated the extent of the damage in the eastern sector of the site during the later phase of the bombings, particularly between September 15 and 18, when at least 10 bombs are documented to have struck the area of the *Palestra Grande* (Angelone and Vitagliano 2020). However, based on aerial photographs taken during the bombardments, it remains difficult to determine with precision the exact locations of the impacts. Further observations on B-scan sections reveal a layered behaviour of the subsurface, with strong interfaces and local slightly sloped reflective surfaces (Figure 13) which can be found at depths ranging from 0.6 to 1.5 m. We infer that these interfaces represent a discontinuity between the exposed Roman paleosol and cinerite deposits left by ancient volcanic activity. The multi-method comparison of GPR and ERT profiles may help assess this, by linking the resolution at shallow depths of GPR and the physical interpretation of resistivity values in ERT.

3.2.3 | Geophysical Data Comparison

ERT data reveal a regular three-layer structure within the upper 10 m, where pronounced high-resistivity anomalies can be observed in the first 2 m b.g.l. of Sections A and B (Figure 9). Whereas Section A exhibits a single, broad resistive anomaly, Section B is characterized by a discontinuous set of features. The GPR survey provides a detailed reconstruction of the near-surface dielectric properties, delivering clear information within the first 2 m b.g.l. The time-slices show a variety of reflections, some of which appear to be functionally associated with the *natatio* located at the centre of the yard. To enhance the interpretative value of the results, a qualitative integration of the two datasets was carried out, which helped clarify the nature of several of the identified features.

In Section A, the resistive zone identified by ERT aligns with a prominent dielectric reflector visible in the 0.3–1.6 m b.g.l.

10990763, 0, Downloaded from https://onlinelibrary.wiley.com/doi/10.1002/arp.70066 by Valentina Santoro - Politecnico Di Torino Sist. Bibl Del Polit Di Torino , Wiley Online Library on [07/10/2026]. See the Terms and Conditions (https://onlinelibrary.wiley.com/terms-and-conditions) on Wiley Online Library for rules of use; OA articles are governed by the applicable Creative Commons License

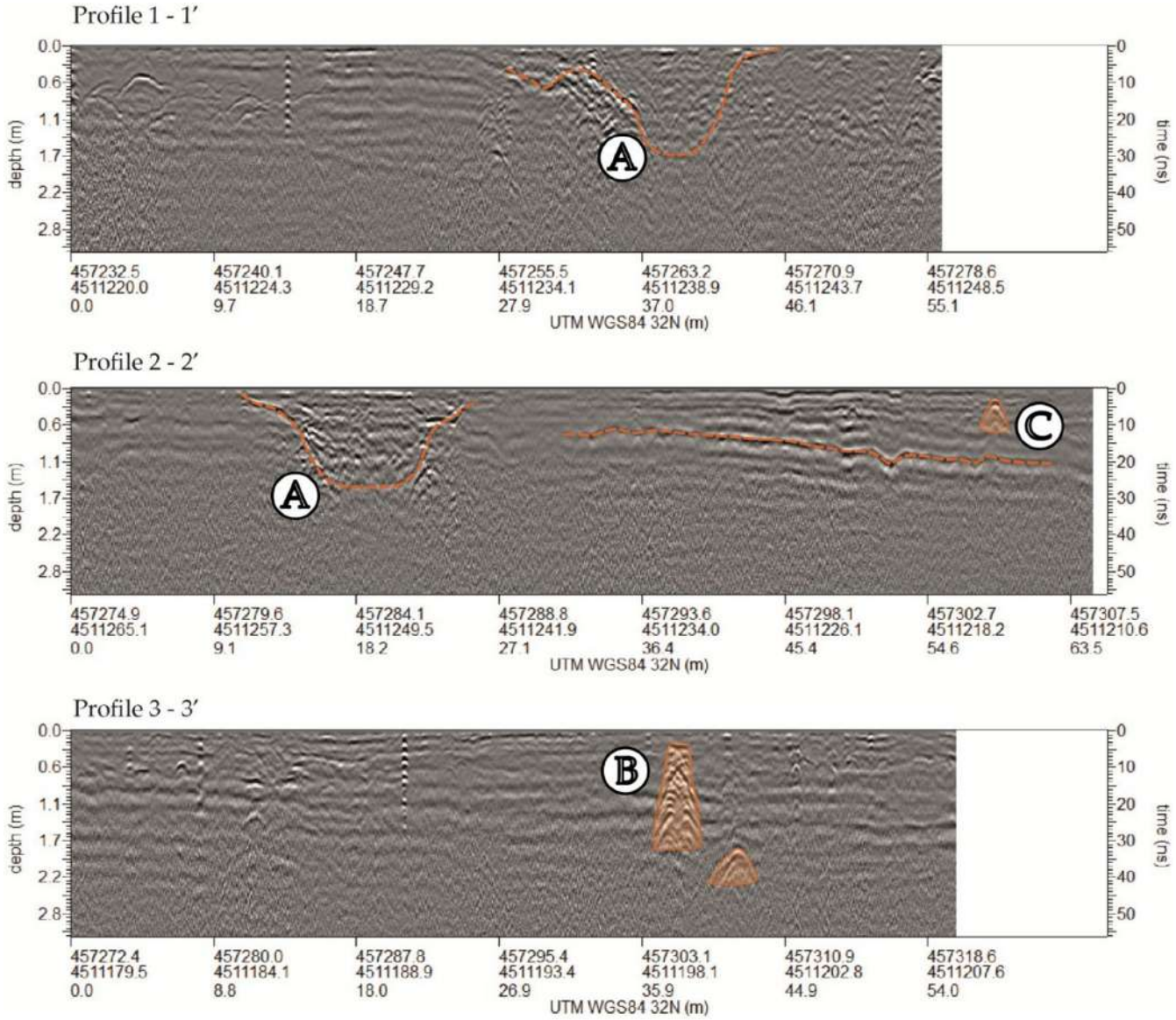


FIGURE 12 | B-scan profiles selected at locations marked in Figure 11. The reflections corresponding to shapes previously noted (A–C) are highlighted in orange.

interval. An initial interpretation based solely on the GPR data—namely, the geometry and intensity of the reflections—suggested that this feature represented a loose material infill, expected to be relatively conductive and associated with reworked deposits. However, the ERT results indicate that the anomaly is in fact resistive. More specifically, the GPR reflections appear to outline the boundary of this resistive body, whereas the material filling its interior produced weak reflections, which had initially led to the assumption of a conductive infill. The integrated interpretation (upper panel of Figure 14) therefore supports the presence of a resistive body whose margins generate strong dielectric contrasts. Furthermore, the progressive increase in conductivity with depth closely mirrors the degradation of the signal-to-noise ratio observed in the GPR data. This pattern is particularly evident in the left portion of the combined dataset section, where a cluster of diffraction hyperbolas appears to delineate the transition between different zones of soil conductivity, possibly reflecting a pedological shift in material composition. Among all the anomalies identified in the survey area, this feature stands out as the most compelling candidate for a bomb crater.

In section B, a clear correspondence between ERT and GPR anomalies can be observed (lower panel of Figure 14). One of the largest linear features detected in the GPR time-slices intersects the ERT profile, where it manifests as a resistive anomaly. This consistency across methods suggests the presence of a subsurface structure with high resistivity (over 1000 Ωm). The GPR response—characterized by multiple, high-amplitude internal reflections—may indicate the presence of air-filled cavities or voided conduits, as such features can produce complex reflection patterns due to strong dielectric contrasts (Lai et al. 2018). A masonry structure cannot be excluded; however, the reflection and resistivity of the anomaly are more consistent with the interpretation of a void or partially voided feature.

10990763, 0, Downloaded from https://onlinelibrary.wiley.com/doi/10.1002/arp.70066 by Valentina Santoro - Politecnico Di Torino Sist. Bibl Del Polit Di Torino , Wiley Online Library on [07/10/2026]. See the Terms and Conditions (https://onlinelibrary.wiley.com/terms-and-conditions) on Wiley Online Library for rules of use; OA articles are governed by the applicable Creative Commons License

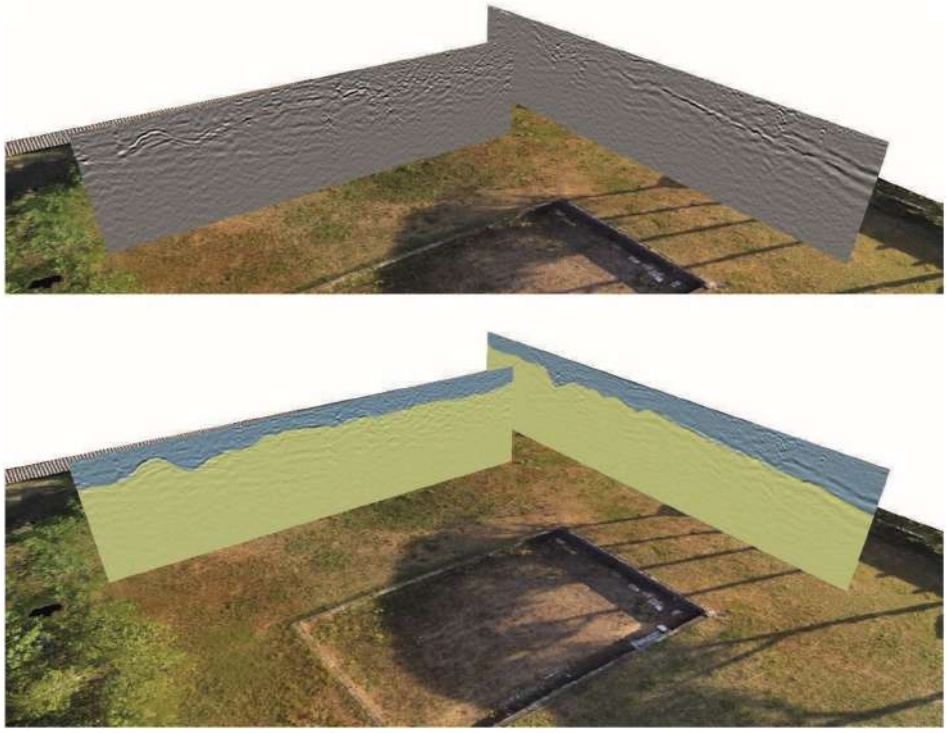


FIGURE 13 | Two representative B-scan sections, which display the layered asset of the subsurface. In the lower panel the same sections are shown with highlighted discontinuities.

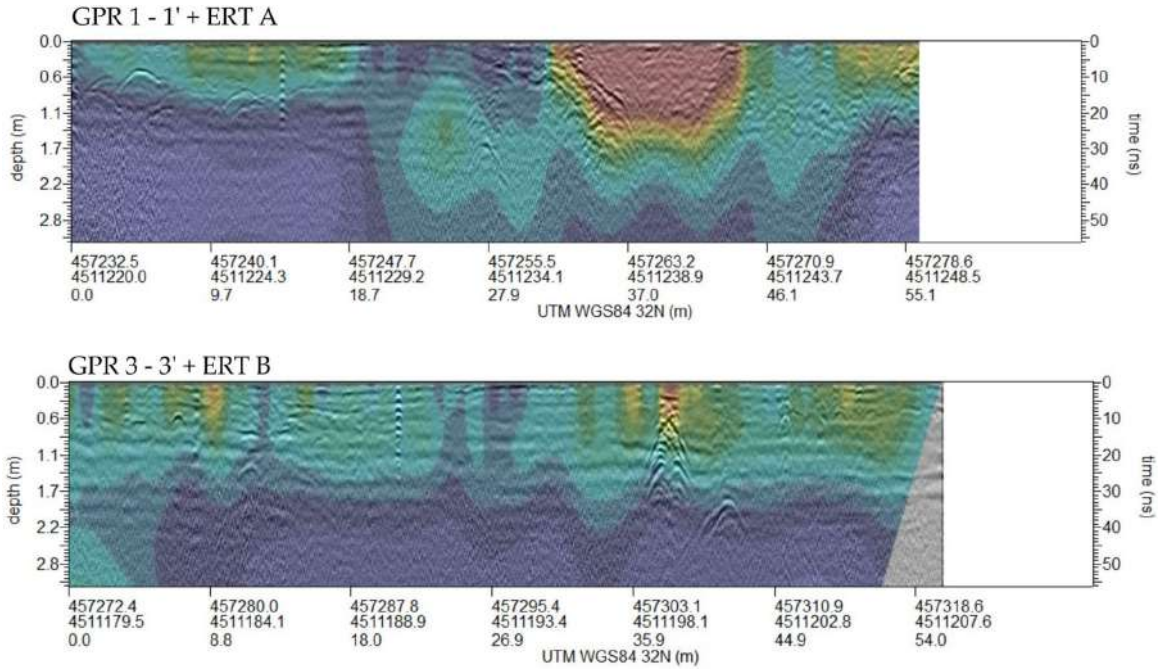


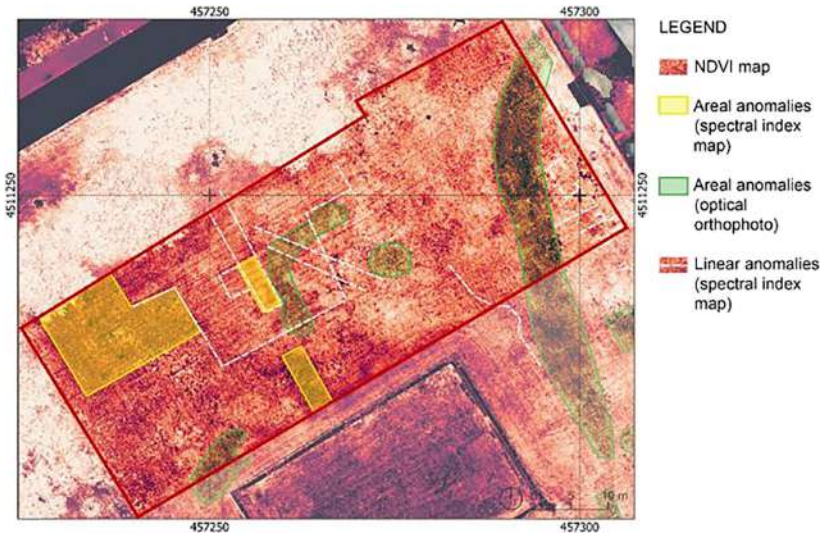
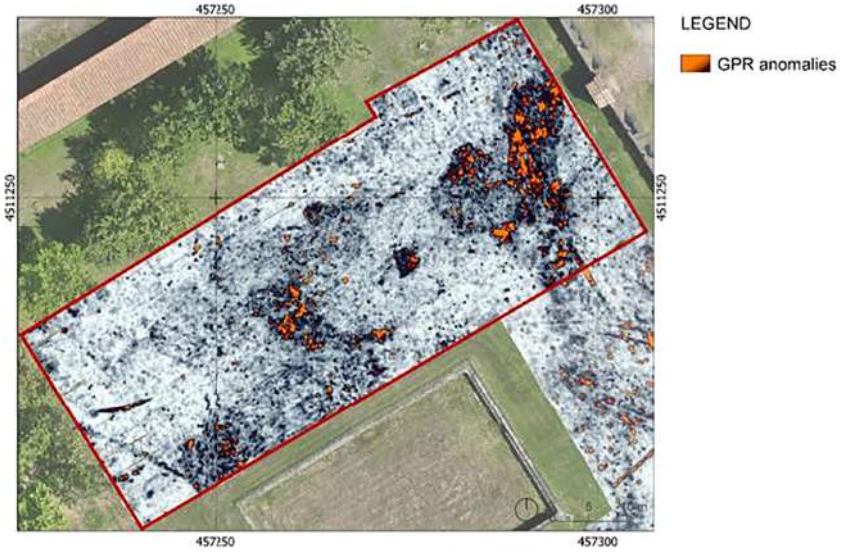
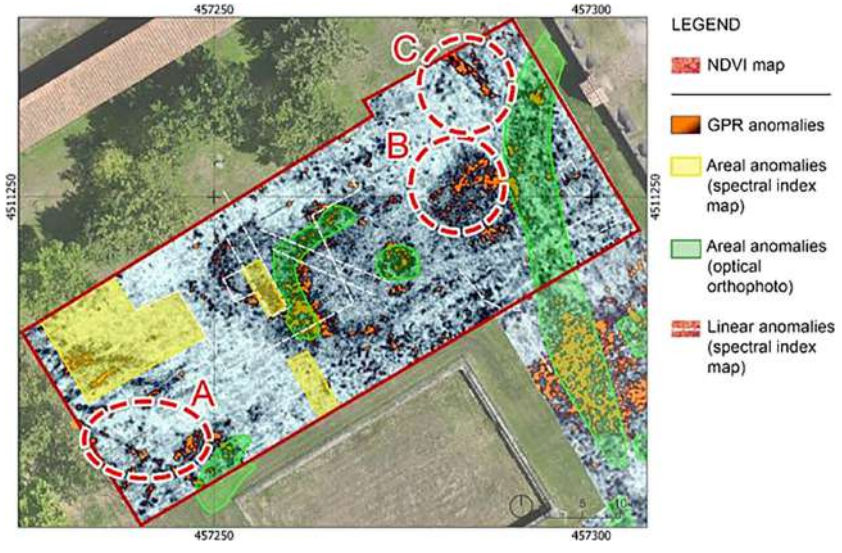
FIGURE 14 | Qualitative integration of ERT and GPR data to enhance and clarify the nature of subsurface features.

4 | Data Integration

Multi-spectral and geophysical data have been jointly analysed within QGIS, through visual interpretation and comparison of the spectral index maps with GPR overlay time-slices within 1 m b.g.l. Additionally, a quantitative approach involving the analysis of the maps derived from both UAV-based and GPR surveys was explored. This attempt aimed at an analytical synthesis of the datasets, with the goal of enhancing the detection and interpretation of potential anomalies. In both cases, the comparison and overlay were conducted exclusively within the central area of the *Palestra Grande* court, which

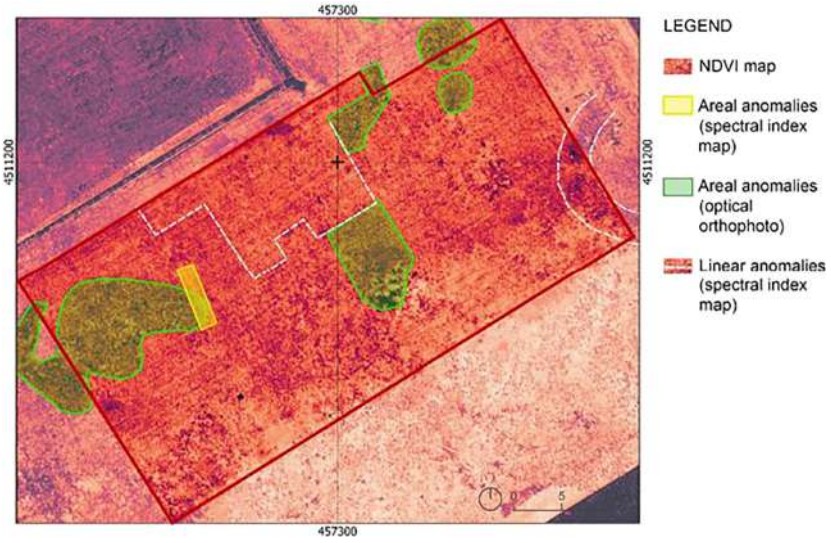
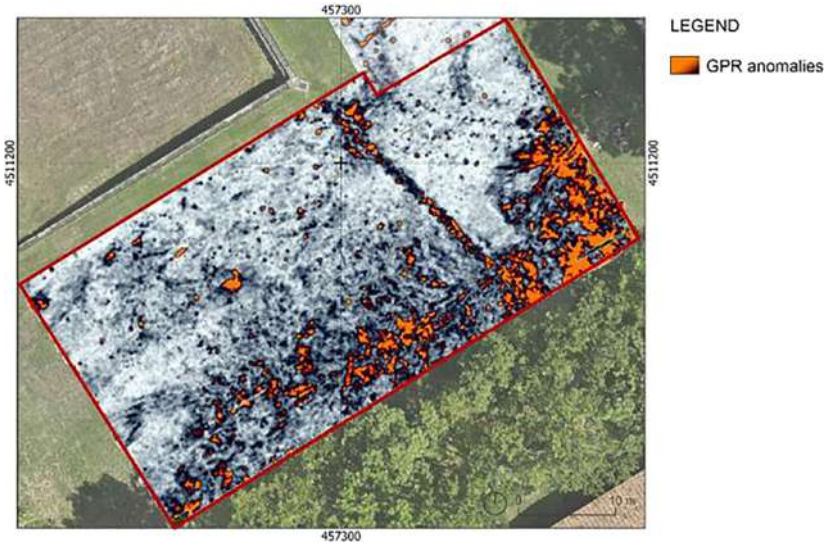
10990763, 0, Downloaded from https://onlinelibrary.wiley.com/doi/10.1002/arp.70066 by Valentina Santoro - Politecnico Di Torino Sist. Bibl Del Polit Di Torino , Wiley Online Library on [07/10/2026]. See the Terms and Conditions (https://onlinelibrary.wiley.com/terms-and-conditions) on Wiley Online Library for rules of use; OA articles are governed by the applicable Creative Commons License

TABLE 4 | Northern area: spectral index-based anomalies, GPR-based anomalies and differences.

	Northern area
Multispectral-based anomalies	
GPR anomalies	
Differences	

10990763, 0, Downloaded from https://onlinelibrary.wiley.com/doi/10.1002/arp.70066 by Valentina Santoro - Politecnico Di Torino Sist. Bibl Del Polit Di Torino , Wiley Online Library on [07/10/2026]. See the Terms and Conditions (https://onlinelibrary.wiley.com/terms-and-conditions) on Wiley Online Library for rules of use; OA articles are governed by the applicable Creative Commons License

TABLE 5 | Southern area: spectral index-based anomalies, GPR-based anomalies and differences.

	Southern area
Multispectral-based anomalies	
GPR anomalies	
Differences	

10990763, 0, Downloaded from https://onlinelibrary.wiley.com/doi/10.1002/arp.70066 by Valentina Santoro - Politecnico Di Torino Sist. Bibl Del Polit Di Torino , Wiley Online Library on [07/10/2026]. See the Terms and Conditions (https://onlinelibrary.wiley.com/terms-and-conditions) on Wiley Online Library for rules of use; OA articles are governed by the applicable Creative Commons License

corresponds to the portion investigated through the GPR survey.

4.1 | Visual Interpretation and Comparison

For the visual interpretation, the multispectral-derived anomalies (shapefile format) have been overlapped with GPR time-slices (TIFF format) individually and then compared. The objective was to assess whether the two analyses produced consistent results. To facilitate the analysis, the *Palestra Grande* courtyard has been divided into three areas. The northern area (Table 4) includes the north-west part of the *Palestra*, whereas the southern area (Table 5) is located in the south-east part of the court. In Tables 4 and 5, the first row displays the spectral anomalies detected in the area and is overlapped on the NDVI map, whereas the second row shows the most relevant and effective time-slices (0–98 cm range of depth), enhancing the detected anomalies in orange shades. The third row includes a schematic representation of the comparison. The central area, on the west side of the *natatio*, is described here, whereas the complete table with all maps and schemes is provided in Appendix S4.

- The northern area (Table 4) shows a good overlapping between the multispectral and visible-based anomalies and the GPR ones, in the central part of the area (e.g., PG2, PG3, PGV9, PGV12), above the *natatio* and also on the east side of the court, where a long irregular anomaly (PGV1) has been detected by both technologies. On the west side, instead, even if the spectral indexes displayed a very clear and regular anomaly (PG1), the GPR showed little result, only detecting a few linear anomalies, concentrated in a corner.

Conversely, three areas (Table 4, third row) reveal discrepancies between the two methodologies, possibly influenced by the surrounding conditions during the survey. In all three cases, the GPR map highlights anomalies that were not readily detectable through the spectral indices. Notably, as illustrated by the Area C example (Figure 15), the NDVI and RN map did reveal some linear anomalies compatible with the one detected by GPR technique; however, probably because of the condition of the vegetation, these were subtle and could not be easily identified.

- In the southern area, a consistency between the spectral index-based and GPR anomalies can be observed (Table 5). However, the GPR revealed two linear and highly energetic anomalies oriented towards the *natatio*, likely connected to the water system. Regarding the first anomaly (on the east side), a comparison between the

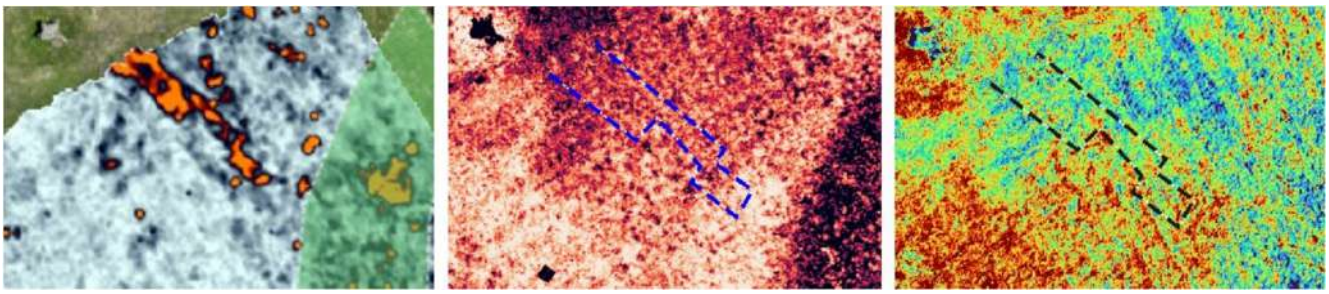


FIGURE 15 | Zoomed-in Area C, illustrating the different detection responses of GPR, NDVI and RN index to the same anomaly, underscoring the methodological variation in anomaly identification.

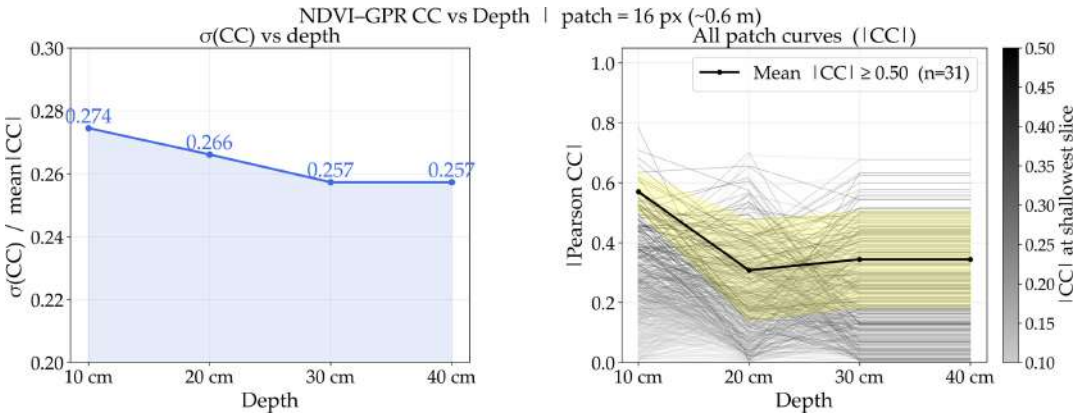


FIGURE 16 | On the left panel, σ(CC)/mean(CC) is represented. The decrease of this trend is a positive indicator that NDVI and GPR data lose correlation in a meaningful way as depth increases. On the right panel, the absolute value of CC is traced against depth. The overall decrease of the signal is indicated by a bold line. Deviations of $\pm 1\sigma$ are shaded in yellow.

10990763, 0, Downloaded from https://onlinelibrary.wiley.com/doi/10.1002/arp.70066 by Valentina Santoro - Politecnico Di Torino Sist. Bibl Del Polit Di Torino , Wiley Online Library on [07/10/2026]. See the Terms and Conditions (https://onlinelibrary.wiley.com/terms-and-conditions) on Wiley Online Library for rules of use; OA articles are governed by the applicable Creative Commons License

GPR and the spectral index maps revealed a partial correspondence, especially closer to the pool (mapped as PGV2 in the visible spectrum) and in the area near the trees. A similar comparison was carried out for the second anomaly (on the west side); however, the results were less conclusive, likely due to the greater depth of the buried feature responsible for the anomaly, which may reduce its influence on surface-level vegetation and, consequently, on the spectral signal.

- The central area displayed a series of correspondences between the anomalies detected by the two methodologies. However, the shape of the anomalies does not completely coincide. This is likely due to the different levels of depth that the two approaches are able to assess. Specifically, multispectral photogrammetry analyses elements that are near the surface or elements that, even if located in great depth, can influence the vegetation and soil above them.

Notably, the linear anomaly detected by GPR did not produce any corresponding response in the spectral index maps. Instead, only small and isolated anomalies were observed in the same area, not easily identifiable without the integrated methodological approach.

In general, although any potential correspondence was expected to occur primarily within the uppermost layers—given the inherently superficial nature of multispectral analysis—the substantial number of matches observed between multispectral and GPR anomalies within the 0–1.00 m depth range beneath the court surface proved to be compelling. Conversely, as anticipated, comparison with anomalies detected at greater depths encountered limitations. The deeper the artefact lies within the soil, the less it will affect the surface vegetation or soil, making it progressively more difficult to detect by its spectral anomalies. In contrast, the GPR method can provide results at greater depths more effectively. The multispectral investigation represents an initial step of analysis, which can be applied on a large scale, extensively, at relatively low cost, detecting spectral anomalies. This approach would allow for a progressive narrowing and refinement of the areas to be analysed, guiding the selection of regions that could be further explored using geophysical methods. The aim is to help identify the most promising and cost-effective areas suitable for archaeological excavations.

4.2 | Cross-Correlation Analysis

The availability of very-high resolution datasets from multispectral photogrammetry and multichannel 3D GPR provided an opportunity to perform data integration that goes beyond the simple overlay of independently interpreted results. The image enhancement strategy adopted here is grounded in a direct physical link: NDVI is sensitive to vegetation vigour and water content, whereas GPR detects subsurface dielectric contrasts that are themselves strongly affected by soil moisture. Buried archaeological features such as walls, floors, voids or infills alter the local water retention capacity of the soil, which in turn influences vegetation growth above them, producing cropmarks visible in the NDVI imagery. By fusing the two datasets through a cross-correlation framework, we aimed to exploit this chain of physical dependencies rather than treating the two surveys independently. Crucially, the strength of this coupling is strongly depth-dependent: It is governed by the extent of the root apparatus of the overlying vegetation, which mediates how deeply subsurface moisture anomalies can influence surface plant responses. Because the *Palestra Grande* yard is predominantly lawn, its root system is expected to be confined to the uppermost tens of centimetres of the soil column, with an estimated maximum rooting depth below 40 cm (Beard 2001). The cross-correlation analysis was therefore designed to test this expectation quantitatively, by measuring at which depth the correlation between GPR and NDVI responses drops below a critical threshold, which is the depth at which the physical link between surface vegetation and subsurface features can be considered severed; beyond this depth, any residual correlation must be attributed to noise.

The spatial correlation analysis between NDVI map and GPR is performed through the calculation of the Pearson cross-correlation coefficient (CC), between the NDVI map and a time-slice stack (extracted from the envelope pulse volume). The results of this analysis are summarized in the two complementary panels of Figure 16.

The left graph shows the standard deviation of CC, σ(CC), over the mean of CC, computed across random patches in the investigated area. After a multi-scale approach to find the optimal patch size, the results displayed here refer to 500 randomly placed 16-pixel windows. The σ(CC) metric carries a quality check of the cross-correlation approach: when the NDVI signal is related to shallow subsurface features, patches that happen to overlap with dielectric anomalies will yield high |CC| values, whereas patches over undisturbed subsurface will yield values close to zero, producing a wide, spread-out distribution and therefore a high σ. As depth of GPR time-slices increases and the radar signal progressively decouples from the surface vegetation pattern, this difference is expected to decrease, giving a more homogenous result. A clear downward trend therefore constitutes statistical evidence that the NDVI and the shallowest GPR time-slices share spatially coherent information.

The right graph shows the absolute value of CC (|CC|) for every individual patch as a function of depth. Each curve traces how the correlation strength of a single patch evolves as depth increases. The shade assigned to each curve is fixed at the value of |CC| that the patch achieved at the shallowest time-slice, and does not change across depths, to visually track whether patches that were strongly coupled to the NDVI signal near the surface, shown in darker tones, tend to maintain or lose that coupling as depth increases, compared with patches that were already weakly correlated at the surface, shown in light grey. Patches exceeding a high-intensity threshold ($|CC| \geq 0.5$ at the shallowest depth) are additionally summarized by a bold trend line with a $\pm 1\sigma$ envelope, which isolates the decay of |CC| in the most strongly coupled patches.

Once the physical link between multispectral and dielectric anomalies was established, we performed a custom image fusion algorithm developed in QGIS. The steps followed to achieve it are summarized in the scheme of Figure 17.

10990763, 0, Downloaded from https://onlinelibrary.wiley.com/doi/10.1002/arp.70066 by Valentina Santoro - Politecnico Di Torino Sist. Bibl Del Polit Di Torino , Wiley Online Library on [07/10/2026]. See the Terms and Conditions (https://onlinelibrary.wiley.com/terms-and-conditions) on Wiley Online Library for rules of use; OA articles are governed by the applicable Creative Commons License

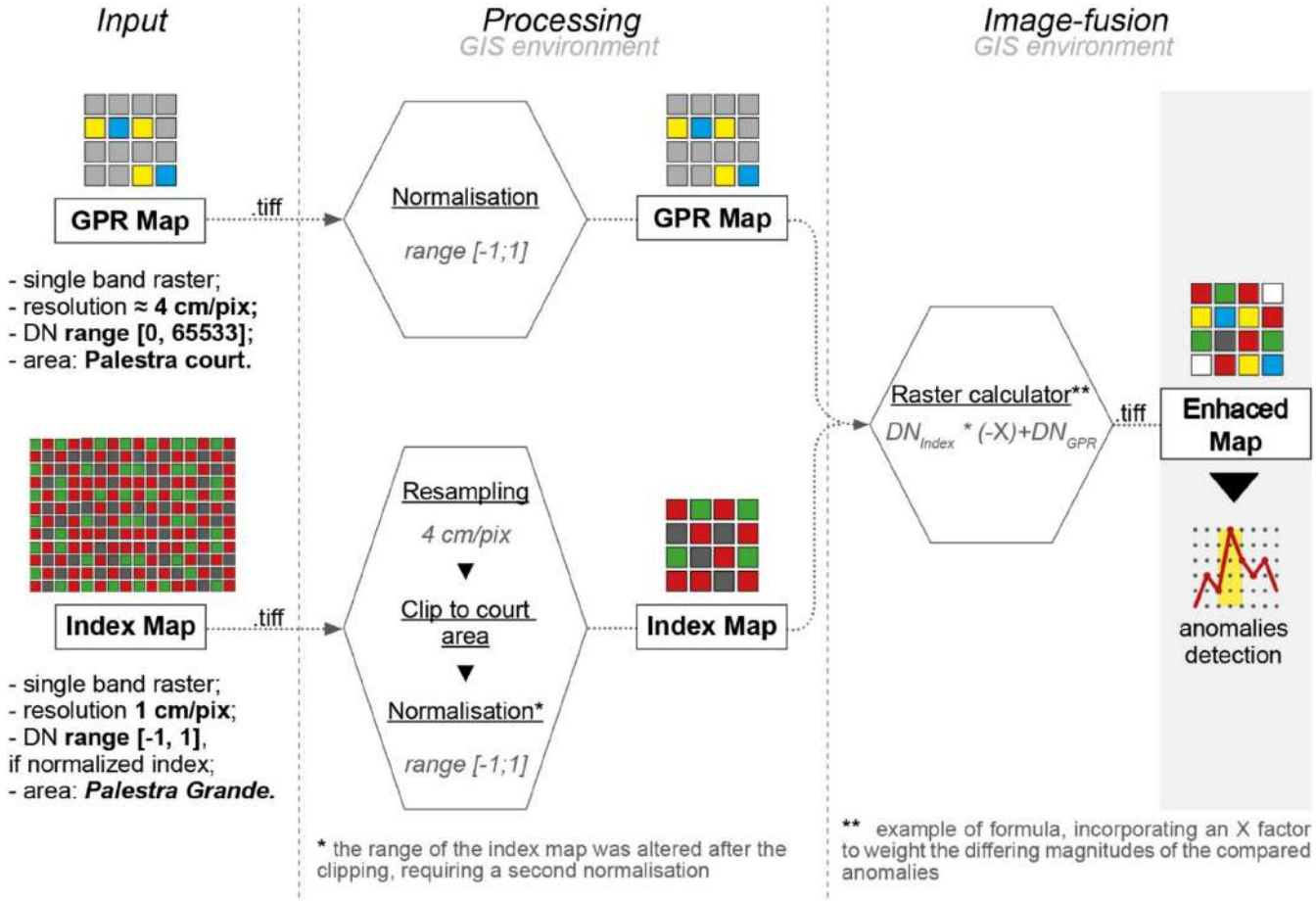


FIGURE 17 | Scheme summarizing the data processing and the final image-fusion map workflow of analysis.

The methodology was tested on a 30-cm GPR time-slice (from the migrated volume) and the NDVI map. Both datasets are single-band rasters, though characterized by differing spatial resolutions, extents and value ranges, as illustrated in the scheme of Figure 16. To harmonize the data and enable direct comparison, the GPR values were normalized to a [−1; 1] scale using the following Equation (1). This transformation also facilitated their comparability with the NDVI values, which are already normalized to the same range.

$$DN_{norm} = 2 \times \left(\frac{DN - DN_{min}}{DN_{max} - DN_{min}} \right) - 1 \quad (1)$$

The NDVI map, instead, underwent spatial resampling to match the cell resolution of the GPR dataset (using the 'mode' resampling method in QGIS). Subsequently, the resulting raster was clipped to retain only the area corresponding to the GPR survey extent. This clipping process required a second normalization of the NDVI map, limited to the values within the newly defined extent.

Following these processing steps, the two harmonized rasters were used as input for the computation of the image-fusion enhanced raster, based on the following Equation (2). Its formulation was selected through preliminary empirical tests in which different combinations of the input raster values and different scaling factors were applied. The resulting maps were visually compared, and the final formulation, including a scaling factor of −2 for the spectral-index values, was selected as the one providing the clearest visual representation of the spatial correspondences between anomalies in the two datasets:

$$Enhanced\ map = \left(DN_{spectral\ index} \times (-2)\right) + DN_{GPR} \quad (2)$$

As shown in Equation (2), the digital number (DN) of the spectral index was multiplied by a numerical factor, as preliminary analyses revealed that the spectral anomalies exhibited a lower magnitude compared with those in the GPR data. Among the tested scaling factors, a factor of 2 provided the clearest visual correspondence between the resulting anomaly patterns. The spectral-index DN values were also multiplied by −1 because the spectral anomalies tended to present an opposite sign relative to those identified in the GPR dataset. The resulting cross-correlation map (Figure 18) represents in false colour the DN derived by the previous calculation.

Specifically, extreme values correspond to areas where anomalies were identified by both spectral index and GPR datasets overlap, whereas values close to 0 indicate areas where the detected anomalies are of very low magnitude, or no anomalies were detected

10990763, 0, Downloaded from https://onlinelibrary.wiley.com/doi/10.1002/arp.70066 by Valentina Santoro - Politecnico Di Torino Sist. Bibl Del Polit Di Torino , Wiley Online Library on [07/10/2026]. See the Terms and Conditions (https://onlinelibrary.wiley.com/terms-and-conditions) on Wiley Online Library for rules of use; OA articles are governed by the applicable Creative Commons License

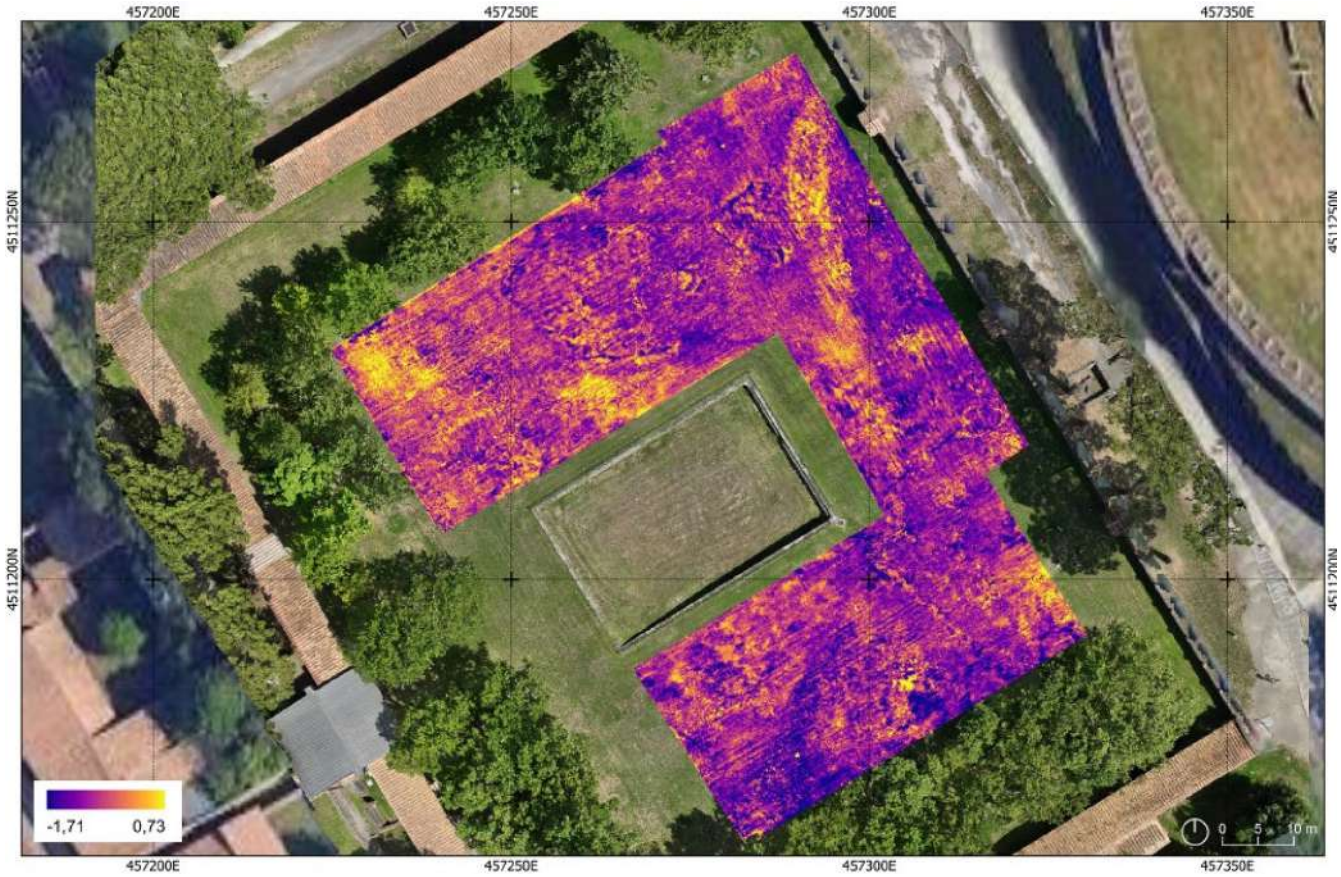


FIGURE 18 | Image-fusion map, enhancing anomalies in [−1.73; 0.73] range of values.

by either method. Intermediate values, instead, are more complex to interpret, as they highlight areas where the contribution in the detection depends on both methods, to varying degrees.

Further analysis was conducted by plotting the DN values from the three involved maps along a specific section (indicated by a black dashed line) in a diagram (Figure 19). This method enabled a more detailed evaluation of both the range and intensity of the investigated values. In the graph (a), the x-axis represents the linear extent of the section in metres, whereas the y-axis displays the DN value range derived from the NDVI index and the GPR dataset, alongside those of the cross-correlation map. This highlights the difference between the datasets by comparing the DN contributions from the two input maps with the corresponding values from the fused map, offering insight into the range of the original datasets and the heterogeneity of anomaly contributions from different sources. The interpretation of the values was further refined through the examination of some previously identified anomalies (Figure 18). Anomaly 1, for instance, was detected through spectral index analysis (highlighted in light blue in the map and in the graphs) and weakly by GPR. Conversely, Anomaly 2 was identified by both spectral index and GPR (highlighted in yellow in the map and in the graphs). By correlating these known anomalies with their corresponding positions in the enhanced map, it was possible to better understand how the two datasets interact and contribute to the detection process.

The findings already suggested by the DN value analysis along the section are further substantiated by these two example anomalies. In fact, they demonstrate that when the detection involves contributions from both methods, the resulting numerical inputs are significantly higher compared with those associated with the detection by a single method. However, it is possible for an anomaly to be strongly detected by only one method and be attributed to the joint effect on both, therefore giving a false positive.

This is particularly relevant given the inherent heterogeneity of the input data, which persists despite efforts to normalize them and enhance their comparability, as Figure 17 shows. As previously noted, the differing range of the anomalies detected by each dataset leads to GPR digital numbers contributing more prominently to the image fusion output, even after adjustments such as rescaling the multispectral data. One possible refinement could involve normalizing the spectral index values (in this case, NDVI) within a narrower interval—specifically where anomalies are more frequently observed—to strengthen their contribution to the analysis.

5 | Archaeological Interpretation of Integrated Anomalies

Beyond the methodological comparison, the integrated analysis also allows some archaeological considerations regarding the nature and possible origin of the detected anomalies. As previously discussed, a realistic interpretation of some of the anomalies detected through the investigations carried out on site

10990763, 0, Downloaded from https://onlinelibrary.wiley.com/doi/10.1002/arp.70066 by Valentina Santoro - Politecnico Di Torino Sist. Bibl Del Polit Di Torino , Wiley Online Library on [07/10/2026]. See the Terms and Conditions (https://onlinelibrary.wiley.com/terms-and-conditions) on Wiley Online Library for rules of use; OA articles are governed by the applicable Creative Commons License

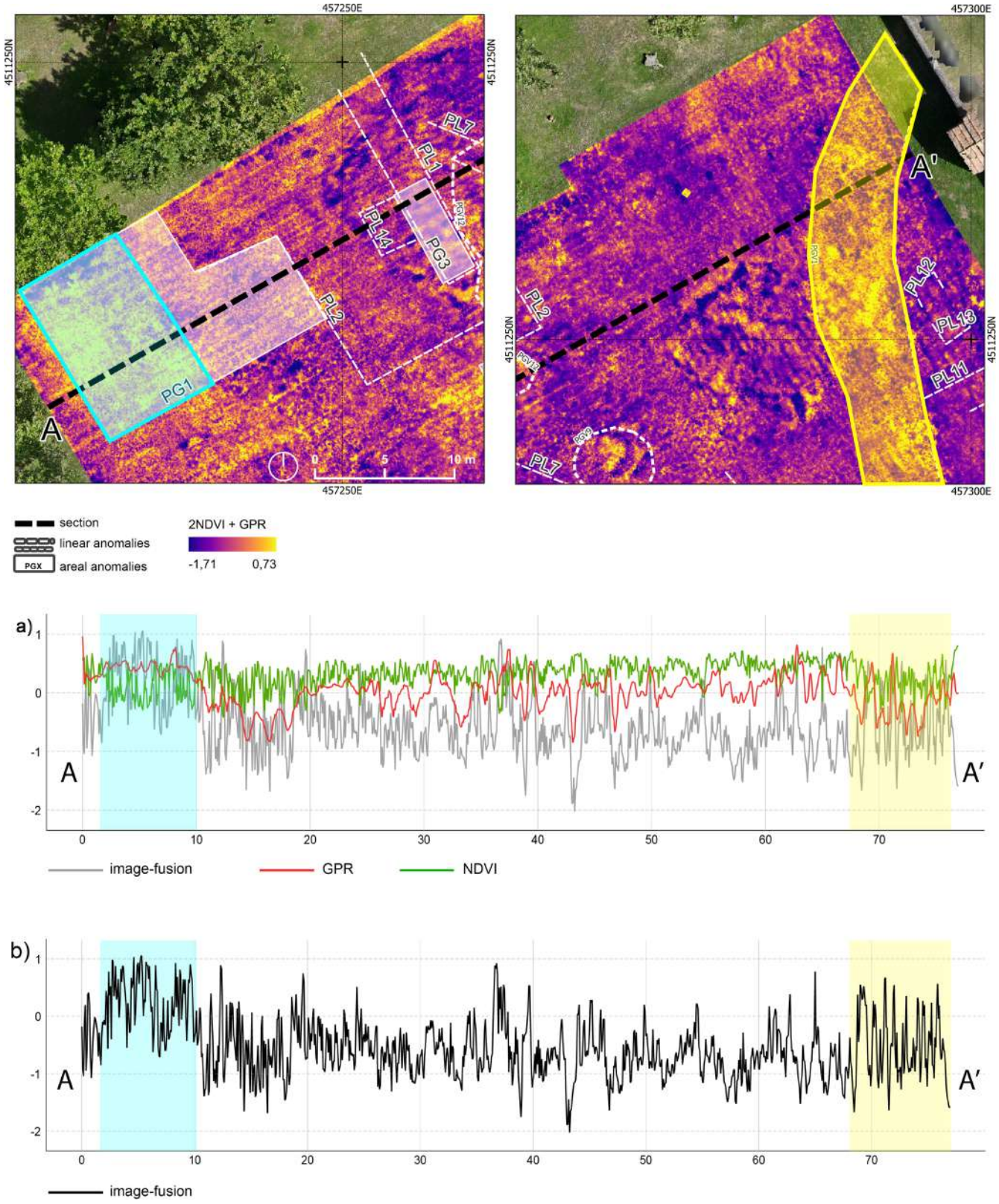


FIGURE 19 | Examples of anomalies detected in the enhanced map, represented in different shades of orange-yellow: left, an anomaly previously detected by spectral index maps, highlighted in light blue; right, an anomaly previously detected by spectral index maps, RGB orthophoto and GPR data, highlighted in yellow. (a) Diagram of comparison between the DN of the three calculated maps: enhanced map, GPR slice (30 cm) and NDVI spectral index; (b) a diagram plotting only the DN on the raster cross-correlation map section A–A′.

10990763, 0, Downloaded from https://onlinelibrary.wiley.com/doi/10.1002/arp.70066 by Valentina Santoro - Politecnico Di Torino Sist. Bibl Del Polit Di Torino , Wiley Online Library on [07/10/2026]. See the Terms and Conditions (https://onlinelibrary.wiley.com/terms-and-conditions) on Wiley Online Library for rules of use; OA articles are governed by the applicable Creative Commons License

may be attributed to the intense bombardments that affected Pompeii and, more specifically, the *Palestra Grande* in 1943. The results of the present study allow the possible bomb-impact points to be identified with substantially greater precision. Our possible interpretation is that these may correspond to several of the circular and oval anomalies detected through multispectral and GPR analyses, including PGV1, PGV8, PGV11 and PL4–PL5 (Figure 7).

Regarding the linear anomalies, these may indicate anthropogenic interventions, either ancient or modern. On the one hand, anomalies extending towards the corners of the pool (e.g., the linear GPR anomaly in Table 5C and the linear spectral Anomaly A in Table 4C) may plausibly be interpreted as channels designed either to convey water collected from the roofs of the surrounding colonnades or, alternatively, to drain water from the pool. On the other hand, PG2 and PG3 appear to be aligned with, and possibly connected to, the water channel whose inspection shaft is visible along Via di Castricio, to the north of the *Palestra Grande* (Figure 7). The interpretation of other anomalies, such as PL2, PL6 and PL7 (Figure 7), remains uncertain; in such cases, targeted archaeological investigation may prove decisive. The possible connection between these anomalies and the structures dismantled to make way for the *Palestra Grande* remains an open question. They may therefore represent traces of features predating the complex itself, preserving a snapshot of the earlier phases of this sector. Another possibility is that they are related to hydraulic infrastructure serving the *Palaestra*: elements that are no longer visible and are not adequately documented, but of which recent excavations have offered a glimpse, as in the case of the large basins identified immediately outside the complex, in the open area shared with the amphitheatre (Iadanza and Toniolo 2022).

6 | Conclusions

The multidisciplinary approach presented in this study offers new opportunities for heritage documentation, site monitoring and archaeological preservation, also supporting the optimisation of excavation strategies, which are often costly and time-consuming. The integration of geomatic and geophysical techniques adopted in the *Palestra Grande* proved particularly effective for the analysis and interpretation of the investigated area, providing a valuable basis for the planning of future archaeological excavations.

In particular, the combined use of GPR surveys and UAV-derived products, including RGB orthophotos, multispectral imagery and spectral index maps, enabled the detection and characterization of anomalies through complementary datasets. The different sensitivities of these methods provided a more comprehensive understanding of the surveyed area and improved the interpretation of recovered subsurface features.

The integrated analyses allowed the localisation of possible bomb-impact points, which are likely associated with several circular and oval anomalies identified within the study area. Furthermore, a number of linear anomalies revealed evidence of anthropogenic modifications that may be related either to hydraulic infrastructures associated with the functioning of the *Palestra Grande* or to occupation phases predating its construction. Although some of these features can plausibly be interpreted as part of ancient drainage systems, others remain difficult to interpret and require targeted archaeological verification.

Our results also suggest a practical and cost-effective workflow applied for archaeological prospection. Multispectral investigations can be employed as a preliminary screening tool, perhaps over large areas, to identify spectral anomalies rapidly and non-invasively. Subsequently, geophysical methods can be focused on selected targets or areas, progressively refining the investigation and optimizing both survey efforts and excavation planning. This integrated strategy maximizes the obtained information and minimizes the field efforts, the costs and, not least, the disturbance to the archaeological context, providing a robust framework for future investigation activities at Pompeii and in similarly archaeological environments.

Whereas the proposed workflow demonstrates the practical value of integrating multispectral and geophysical investigations, the results also provide an opportunity to assess the strengths and limitations of the analytical procedures adopted in this study. Compared with visual interpretation, the cross-correlation method—despite requiring computational effort and normalization—produces more immediate results when strong, well-defined anomalies are present. However, it is less effective in detecting subtler patterns, which are often more readily identified through visual inspection combined with raster stretching techniques. This limitation highlights a promising direction for future methodological development, particularly through the integration of machine learning or deep learning approaches. Such enhancements would be especially beneficial considering that the proposed methodology is designed to be adaptable to other heterogeneous and potentially larger datasets, where both computational demands and application opportunities are expected to increase. Nevertheless, the results obtained in the present study already demonstrate the reliability of the approach, as the comparison between the archaeological and geomatic/geophysical approaches provides an important validation of the proposed methodology.

The integrated analyses enabled the localisation of several circular, oval and linear anomalies, some of which may correspond to bomb-impact craters, hydraulic infrastructures or features predating the construction of the *Palestra Grande*. However, their definitive interpretation will require targeted archaeological verification.

Acknowledgements

The authors wish to thank Dr. Gabriel Zuchtriegel, Director General of the Archaeological Park of Pompeii, for supporting this research; Dr. Valeria Amoretti for coordinating the agreement with the Park; and Dr. Silvia Martina Bertesago and Dr. Ilaria Cangiano for their support and collaboration during the research activities conducted at the *Palestra Grande*. Open access publishing facilitated by Universita degli Studi di Torino, as part of the Wiley - CRUI-CARE agreement.

Funding

The authors have nothing to report.

10990763, 0, Downloaded from https://onlinelibrary.wiley.com/doi/10.1002/arp.70066 by Valentina Santoro - Politecnico Di Torino Sist. Bibl Del Polit Di Torino , Wiley Online Library on [07/10/2026]. See the Terms and Conditions (https://onlinelibrary.wiley.com/terms-and-conditions) on Wiley Online Library for rules of use; OA articles are governed by the applicable Creative Commons License

Conflicts of Interest

The authors declare no conflicts of interest.

Data Availability Statement

The authors promote and encourage the reuse, implementation and modification of any code, data and method presented in this paper. Supporting material (which is available at the present repository: https://doi.org/10.5281/zenodo.20817026) include:

1. Raw and processed geophysical data (ERT, GPR).
2. RGB and multispectral orthophotos; digital surface model.

References

Adler-Golden, S. M., M. W. Matthew, G. P. Anderson, G. W. Felde, and J. A. Gardner. 2002. "Algorithm for De-Shadowing Spectral Imagery." In *Imaging Spectrometry VIII*, vol. 4816, 203–210. SPIE. https://doi.org/10.1117/12.451691.

Agapiou, A., D. D. Alexakis, A. Sarris, and D. G. Hadjimitsis. 2013. "Orthogonal Equations of Multi-Spectral Satellite Imagery for the Identification of Un-Excavated Archaeological Sites." *Remote Sensing* 5, no. 12: 6560–6586. https://doi.org/10.3390/rs5126560.

Agapiou, A., and D. G. Hadjimitsis. 2011. "Vegetation Indices and Field Spectroradiometric Measurements for Validation of Buried Architectural Remains: Verification Under Area Surveyed With Geophysical Campaigns." *Journal of Applied Remote Sensing* 5, no. 1: 053554. https://doi.org/10.1117/1.3645590.

Agapiou, A., and D. Skarlatos. 2023. "Geomatic Sensors for Heritage Documentation: A Meta-Analysis of the Scientific Literature." *Heritage* 6, no. 10: 6843–6861. https://doi.org/10.3390/heritage6100357.

Agisoft LLC. 2025. *Radiometric Calibration Using the "Use Sun Sensor" Option*. Agisoft Metashape Forum Technical Support, response by A. Pasumansky, 6 May 2025.

Aldrete, G. S. 2004. *Daily Life in the Roman City: Rome, Pompeii, and Ostia*. Greenwood Press. https://doi.org/10.5040/9798400637193.

Angelone, G., and G. Vitagliano. 2020. *Just West of Pompeii. Il Sito Archeologico e i Bombardamenti Dell'Estate 1943*. YCP.

Anguissola, A., and R. Olivito. 2022. *Edizione Degli Scavi nei Praedia di Iulia Felix e Studi Sulla Regio II di Pompei. PRAEDIA 1*. Pisa University Press.

Anguissola, A., and R. Olivito. 2023. "Il Progetto PRAEDIA: Le Campagne 2021-2023 nel Complesso dei Riti Magici (II 1, 11-12)." *Rivista di Studi Pompeiani* 34: 221–226.

Anguissola, A., and R. Olivito. 2024. "Il Progetto PRAEDIA: Le Campagne 2023-2024 nel Complesso dei Riti Magici (II 1, 11-12) e le Indagini Diagnostiche Nella Palestra Grande." *Rivista di Studi Pompeiani* 35: 122–130.

Anguissola, A., and R. Olivito. 2025. "Il Progetto PRAEDIA nel Complesso dei Riti Magici (II 1, 11-12): Storia Edilizia e Tracce del Sacro." *Rivista di Studi Pompeiani* 36: 195–203.

Balkaya, Ç., Y. L. Ekinci, O. Çakmak, M. Blömer, J. Arnkens, and M. A. Kaya. 2021. "A Challenging Archaeo-Geophysical Exploration Through GPR and ERT Surveys on the Keber Tepe, City Hill of Doliche, Commagene (Gaziantep, SE Turkey)." *Journal of Applied Geophysics* 186: 104272. https://doi.org/10.1016/j.jappgeo.2021.104272.

Banerjee, B. P., S. Raval, and P. J. Cullen. 2020. "UAV-Hyperspectral Imaging of Spectrally Complex Environments." *International Journal of Remote Sensing* 41, no. 11: 4136–4159. https://doi.org/10.1080/01431161.2020.1714771.

Beard, J. B. 2001. "Turfgrass Root Basics." *Turfax* 9, no. 3: 4–5.

Bennett, R., K. Welham, R. A. Hill, and A. L. Ford. 2012. "The Application of Vegetation Indices for the Prospection of Archaeological Features in Grass-Dominated Environments." *Archaeological Prospection* 19, no. 3: 209–218.

Binley, A., and A. Kemna. 2005. "DC Resistivity and Induced Polarization Methods." In *Hydrogeophysics*, 129–156. Springer.

Blanchy, G., S. Saneiyan, J. Boyd, P. McLachlan, and A. Binley. 2020. "ResIPy, an Intuitive Open Source Software for Complex Geoelectrical Inversion/Modeling." *Computers and Geosciences* 137: 104423. https://doi.org/10.1016/j.cageo.2020.104423.

Bornik, A., and W. Neubauer. 2022. "3D Visualization Techniques for Analysis and Archaeological Interpretation of GPR Data." *Remote Sensing* 14, no. 7: 1709. https://doi.org/10.3390/rs14071709.

Centro Funzionale Multirischi di Protezione Civile Regione Campania. 2023. "Archivio Pluviometrico." https://centrofunzionale.regione.campania.it/#/pages/sensori/archivio-pluviometrici.

Chiabrando, F., F. D'Andria, G. Sammartano, and A. Spanò. 2018. "UAV Photogrammetry for Archaeological Site Survey. 3D Models at the Hierapolis in Phrygia (Turkey)." *Virtual Archaeology Review* 9: 18. https://doi.org/10.4995/var.2018.5958.

Chiabrando, F., A. Lingua, and M. Piras. 2013. "Direct Photogrammetry Using Uav: Tests and First Results." *International Archives of the Photogrammetry, Remote Sensing and Spatial Information Sciences* XL-1/W2: 81–86. https://doi.org/10.5194/isprsarchives-XL-1-W2-81-2013.

Comina, C., R. Leone, I. Palmisano, and A. Vergnano. 2025. "Off-Line Stacking for Multichannel GPR Processing in Clay-Rich Archaeological Sites: The Case Study of Tindari (Sicily)." *Applied Sciences* 15, no. 13: 7157. https://doi.org/10.3390/xxxxx.

Constable, S. C., R. L. Parker, and C. G. Constable. 1987. "Occam's Inversion; a Practical Algorithm for Generating Smooth Models From Electromagnetic Sounding Data." *Geophysics* 52, no. 3: 289–300. https://doi.org/10.1190/1.1442303.

Corradini, E., D. Groß, T. Wunderlich, et al. 2022. "Finding Mesolithic Sites: A Multichannel Ground-Penetrating Radar (GPR) Investigation at the Ancient Lake Duvensee." *Remote Sensing* 14, no. 3: 781. https://doi.org/10.3390/rs14030781.

Dragomir, L. O., P. D. E. C. H. Petrosani, and S. Oncia. 2012. "Using Satellite Images LANDSAT TM for Calculating Normalized Difference Indexes for the Landscape of Parang Mountains, RevCAD." *Journal of Geodesy and Cadastre* 13: 158–167. Universitatea (1° Decembrie 1918) din Alba Iulia. https://www.academia.edu/89624425/Using_Satellite_Images_Landsat_TM_for_Calculating_Normalized_Difference_Indexes_for_the_Landscape_of_Par%C3%A2ng_Mountains.

Filzwieser, R., L. H. Olesen, W. Neubauer, et al. 2017. "Large-Scale Geophysical Archaeological Prospection Pilot Study at Viking Age and Medieval Sites in West Jutland, Denmark." *Archaeological Prospection* 24, no. 4: 373–393. https://doi.org/10.1002/arp.1576.

Forte, M., I. Trinks, A. Hinterleitner, et al. 2022. "Multimodal Remote Sensing Applications in the Etruscan-Roman City of Vulci." *Journal of Field Archaeology* 47, no. 8: 501–521. https://doi.org/10.1080/00934690.2022.2126920.

Fraser, B. T., and R. G. Congalton. 2021. "Monitoring Fine-Scale Forest Health Using Unmanned Aerial Systems (UAS) Multispectral Models." *Remote Sensing* 13, no. 23: 23. https://doi.org/10.3390/rs13234873.

Geuzaine, C., and J. F. Remacle. 2009. "Gmsh: A 3-D Finite Element Mesh Generator With Built-In Pre- and Post-Processing Facilities." *International Journal for Numerical Methods in Engineering* 79, no. 11: 1309–1331. https://doi.org/10.1002/nme.2579.

10990763, 0, Downloaded from https://onlinelibrary.wiley.com/doi/10.1002/arp.70066 by Valentina Santoro - Politecnico Di Torino Sist. Bibl Del Polit Di Torino , Wiley Online Library on [07/10/2026]. See the Terms and Conditions (https://onlinelibrary.wiley.com/terms-and-conditions) on Wiley Online Library for rules of use; OA articles are governed by the applicable Creative Commons License

Glenn, E. P., A. R. Huete, P. L. Nagler, and S. G. Nelson. 2008. "Relationship Between Remotely-Sensed Vegetation Indices, Canopy Attributes and Plant Physiological Processes: What Vegetation Indices Can and Cannot Tell Us About the Landscape." *Sensors* 8, no. 4: 2136–2160. https://doi.org/10.3390/s8042136.

Goetz, A. F. 2009. "Three Decades of Hyperspectral Remote Sensing of the Earth: A Personal View." *Remote Sensing of Environment* 113: S5–S16.

Gojda, M., and M. Hejcman. 2012. "Cropmarks in Main Field Crops Enable the Identification of a Wide Spectrum of Buried Features on Archaeological Sites in Central Europe." *Journal of Archaeological Science* 39, no. 6: 1655–1664. https://doi.org/10.1016/j.jas.2012.01.023.

Goodman, D. 2008. "GPR Methods for Archaeology." In *Seeing the Unseen. Geophysics and Landscape Archaeology*, 255–270. Taylor and Francis Group.

Hill, A. C., E. J. Laugier, and J. Casana. 2020. "Archaeological Remote Sensing Using Multi-Temporal, Drone-Acquired Thermal and Near Infrared (NIR) Imagery: A Case Study at the Enfield Shaker Village, New Hampshire." *Remote Sensing* 12: 4. https://doi.org/10.3390/rs12040690.

Iadanza, M., and L. Toniolo. 2022. "Le Indagini nel Quadrante Sud-Orientale di Pompei: Un Quadro Delle Risultanze." In *Edizione Degli Scavi nei Praedia di Iulia Felix e Studi Sulla Regio II di Pompei*, 77–120. Pisa University Press. https://www.academia.edu/95674889/A_Anguissola_R_Olivito_PRAEDIA_I_Edizione_degli_scavi_nei_Praedia_di_Iulia_Felix_e_studi_sulla_Regio_II_di_Pompei_Pisa_University_Press_Pisa_2022.

Jiang, Z., A. R. Huete, K. Didan, and T. Miura. 2008. "Development of a Two-Band Enhanced Vegetation Index Without a Blue Band." *Remote Sensing of Environment* 112, no. 10: 3833–3845. https://doi.org/10.1016/j.rse.2008.06.006.

Kaimaris, D. 2024. "Aerial Remote Sensing Archaeology—A Short Review and Applications." *Land* 13, no. 7: icolo 7. https://doi.org/10.3390/land13070997.

Karaoulis, M., G. N. Tsokas, P. Tsourlos, P. Bogiatzis, and G. Vargemezis. 2025. "3D Electrical Resistivity Tomography Using a Radial Array and Detailed Topography for Tumuli Prospection." *Archaeological Prospection* 32, no. 1: 197–208. https://doi.org/10.1002/arp.1966.

Keiller, A., and O. G. S. Crawford. 1928. *Wessex From the Air*. Clarendon Press.

Lai, W. W. L., R. Chang, and J. Sham. 2018. *Detection and Imaging of City's Underground Void by GPR*, 1–6. IEEE. https://doi.org/10.1109/IWAGPR.2017.7996055.

Lasaponara, R., N. Masini, and G. Scardozzi. 2007. "Immagini Satellitari ad Alta Risoluzione e Ricerca Archeologica: Applicazioni e Casi di Studio con Riprese Pancromatiche e Multispettrali di QuickBird." *Archeologia e Calcolatori* 18: 187–227.

Ling, R. 2007. "Development of Pompeii's Public Landscape in the Roman Period." In *The World of Pompeii*, edited by J. J. Dobbins and P. W. Foss, 123–132. Routledge.

Lippolis, C., V. Messina, G. Patrucco, V. Santoro, A. Spano, and J. Fassbinder. 2025. *Preliminary Report on the Campaigns 2022–2023 of the Italian Archaeological Expedition at Seleucia on the Tigris (IAES)*. Apice libri. https://iris.polito.it/handle/11583/2997480.

Loke, M. H., and R. D. Barker. 1995. "Least-Squares Deconvolution of Apparent Resistivity Pseudosections." *Geophysics* 60, no. 6: 1682–1690. https://doi.org/10.1190/1.1443900.

Maiuri, A. 1939. *Regione I (Lativm et Campania). I. – Pompei. – Scavo Della "Grande Palestra" nel Quartiere Dell'Anfiteatro (a. 1935–1939)*, 165–238. Apice Libri.

Marchetti, M., V. Materni, V. Sapia, and S. Urbini. 2022. "Indagini Geofisiche Nell'Hortus dei Praedia di Iulia Felix." In *Edizione Degli Scavi nei Praedia di Iulia Felix e Studi Sulla Regio II di Pompei*, 9–14. Pisa University Press. https://www.academia.edu/95674889/A_Anguissola_R_Olivito_PRAEDIA_I_Edizione_degli_scavi_nei_Praedia_di_Iulia_Felix_e_studi_sulla_Regio_II_di_Pompei_Pisa_University_Press_Pisa_2022.

Marx, A., A. Clasen, J. May, S. König, B. Kleinschmit, and M. Förster. 2024. "Imaging Spectroscopy for Bark Beetle Detection in Norway Spruce and the Relevance of the Red-Edge Spectral Range." *International Journal of Applied Earth Observation and Geoinformation* 133: 104100. https://doi.org/10.1016/j.jag.2024.104100.

Matsushita, B., W. Yang, J. Chen, Y. Onda, and G. Qiu. 2007. "Sensitivity of the Enhanced Vegetation Index (EVI) and Normalized Difference Vegetation Index (NDVI) to Topographic Effects: A Case Study in High-Density Cypress Forest." *Sensors* 7, no. 11: 2636–2651. https://doi.org/10.3390/s7112636.

Monterroso-Checa, A., T. Teixidó, M. Gasparini, et al. 2019. "Use of Remote Sensing, Geophysical Techniques and Archaeological Excavations to Define the Roman Amphitheater of Torreparedones (Córdoba, Spain)." *Remote Sensing* 11, no. 24: 2937. https://doi.org/10.3390/rs11242937.

Moriarty, C., D. C. Cowley, T. Wade, and C. J. Nichol. 2019. "Deploying Multispectral Remote Sensing for Multi-Temporal Analysis of Archaeological Crop Stress at Ravenshall, Fife, Scotland." *Archaeological Prospection* 26, no. 1: 33–46. https://doi.org/10.1002/arp.1721.

Neubauer, W., A. Eder-Hinterleitner, S. Seren, and P. Melichar. 2002. "Georadar in the Roman Civil Town Carnuntum, Austria: An Approach for Archaeological Interpretation of GPR Data." *Archaeological Prospection* 9: 135–156. https://doi.org/10.1002/arp.183.

Niu, Z., H. Xia, P. Tao, and T. Ke. 2024. "Accuracy Assessment of UAV Photogrammetry System with RTK Measurements for Direct Georeferencing." *ISPRS Annals of the Photogrammetry, Remote Sensing and Spatial Information Sciences* X-1-2024: 169–176. https://doi.org/10.5194/isprs-annals-X-1-2024-169-2024.

Opitz, R., and J. Herrmann. 2018. "Recent Trends and Long-Standing Problems in Archaeological Remote Sensing." *Journal of Computer Applications in Archaeology* 1, no. 1: 19–41.

Orlando, L., L. M. Michetti, B. Belelli Marchesini, P. Papeschi, and F. Giannino. 2019. "Dense Georadar Survey for a Large-Scale Reconstruction of the Archaeological Site of Pyrgi (Santa Severa, Rome)." *Archaeological Prospection* 26, no. 4: 369–377. https://doi.org/10.1002/arp.1750.

Parslow, C. C. 2007. "Entertainment." In *The World of Pompeii*, edited by J. J. Dobbins and P. W. Foss, 321–335. Routledge.

Patrucco, G., G. Cortese, F. Giulio Tonolo, and A. Spanò. 2020. "Thermal and Optical Data Fusion Supporting Built Heritage Analyses." *International Archives of the Photogrammetry, Remote Sensing and Spatial Information Sciences* XLIII-B3–2020: 619–626. XXIV ISPRS Congress, Commission III (Volume XLIII-B3–2020) - 2020 edition. https://doi.org/10.5194/isprs-archives-XLIII-B3-2020-619-2020.

Pesando, F., and P. Guidobaldi. 2006. *Pompei, Oplontis, Ercolano, Stabiae*. Laterza.

Pons, X., and J.-C. Padró. 2021. "An Operational Radiometric Correction Technique for Shadow Reduction in Multispectral UAV Imagery." *Remote Sensing* 13, no. 19: 3808. https://doi.org/10.3390/rs13193808.

Porcelli, F., L. Sambuelli, C. Comina, et al. 2020. "Integrated Geophysics and Geomatics Surveys in the Valley of the Kings." *Sensors* 20, no. 6: 6. https://doi.org/10.3390/s20061552.

Radicioni, F., A. Stoppini, G. Tosi, and L. Marconi. 2021. "Necropolis of Palazzone in Perugia: Geomatic Data Integration for 3D Modeling and Geomorphology of Underground Sites." *Transactions in GIS* 25: 2553–2570. https://doi.org/10.1111/tgis.12818.

10990763, 0, Downloaded from https://onlinelibrary.wiley.com/doi/10.1002/arp.70066 by Valentina Santoro - Politecnico Di Torino Sist. Bibl Del Polit Di Torino , Wiley Online Library on [07/10/2026]. See the Terms and Conditions (https://onlinelibrary.wiley.com/terms-and-conditions) on Wiley Online Library for rules of use; OA articles are governed by the applicable Creative Commons License

Rana, M. M. S. P., M. T. Rahman, and M. F. Hassan. 2025. "Mapping Groundwater Potential Zone by Robust Machine Learning Algorithms & Remote Sensing Techniques in Agriculture Dominated Area, Bangladesh." *Cleaner Water* 3: 100064. https://doi.org/10.1016/j.clwat.2025.100064.

Rouse, J. W., R. H. Haas, J. A. Schell, and D. W Deering. 1974. "Monitoring Vegetation Systems in the Great Plains With ERTS." NASA. Goddard Space Flight Center 3d ERTS-1 Symp., Vol. 1, Sect. A. https://ntrs.nasa.gov/citations/19740022614.

Russolillo, A., F. F. Martin, A. Merico, et al. 2024. "Unveiling a Hidden Fortification System at "Faraglioni" Middle Bronze Age Village of Ustica Island (Palermo, Italy) Through ERT and GPR Prospections." *Journal of Applied Geophysics* 220: 105272. https://doi.org/10.1016/j.jappgeo.2023.105272.

Salgado Carmona, J. Á., E. Quirós, V. Mayoral, and C. Charro. 2020. "Assessing the Potential of Multispectral and Thermal UAV Imagery From Archaeological Sites. A Case Study From the Iron Age Hillfort of Villasviejas del Tamuja (Cáceres, Spain)." *Journal of Archaeological Science: Reports* 31: 102312. https://doi.org/10.1016/j.jasrep.2020.102312.

Sammartano, G., F. Chiabrando, and A. Spanò. 2020. "Oblique Images and Direct Photogrammetry With a Fixed Wing Platform: First Test and Results in Hierapolis of Phrygia (TK)." *International Archives of the Photogrammetry, Remote Sensing and Spatial Information Sciences* XLIII-B2–2020: 75–82. XXIV ISPRS Congress, Commission II (Volume XLIII-B2–2020) - 2020 edition. https://doi.org/10.5194/isprs-archives-XLIII-B2-2020-75-2020.

Santoro, V., Z. Wu, G. Patrucco, and A. Spanò. 2026. "Investigations of Non-Visible Features in Archaeological Sites: Testing Aerial Remote Sensing With UAV in Pompeii." *Virtual Archaeology Review* 17, no. 34: 1–25. https://doi.org/10.4995/var.2024.24163.

Sapia, V., F. Villani, F. Fischanger, et al. 2021. "3-D Deep Electrical Resistivity Tomography of the Major Basin Related to the 2016 M_w 6.5 Central Italy Earthquake Fault." *Tectonics* 40, no. 4: e2020TC006628. https://doi.org/10.1029/2020TC006628.

Schmiedt, G. 1957. *Applicazioni Della Fotografia Aerea in Ricerche Estensive di Topografia Antica in Sicilia*, vol. 3, 18–30. Kokalos.

Shukla, T., W. Tang, C. C. Trettin, G. Chen, S. Chen, and C. Allan. 2023. "Quantification of Microtopography in Natural Ecosystems Using Close-Range Remote Sensing." *Remote Sensing* 15: 9. https://doi.org/10.3390/rs15092387.

Sigurdsson, H., S. Cashdollar, and S. R. Sparks. 1982. "The Eruption of Vesuvius in AD 79: Reconstruction From Historical and Volcanological Evidence." *American Journal of Archaeology* 86, no. 1: 39–51.

Stal, C., K. Van Liefferinge, J. De Reu, et al. 2014. "Integrating Geomatics in Archaeological Research at the Site of Thorikos (Greece)." *Journal of Archaeological Science* 45: 112–125.

Tejero-Andrade, A., D. L. Argote-Espino, G. Cifuentes-Nava, E. Hernández-Quintero, R. E. Chávez, and A. García-Serrano. 2018. "'Illuminating' the Interior of Kukulkan's Pyramid, Chichén Itzá, Mexico, by Means of a Non-Conventional ERT Geophysical Survey." *Journal of Archaeological Science* 90: 1–11. https://doi.org/10.1016/j.jas.2017.12.006.

Trinks, I., and A. Hinterleitner. 2020. "Beyond Amplitudes: Multi-Trace Coherence Analysis for Ground-Penetrating Radar Data Imaging." *Remote Sensing* 12, no. 10: 1583. https://doi.org/10.3390/rs12101583.

Urbini, S., V. Sapia, V. Materni, et al. 2021. *Indagini Geofisiche Nell'Hortus dei Praedia Iuliae Felicis (Pompei, II, 4). Risultati Preliminari e Prospettive*. Archaeologica data volume 1. All'Insegna del. https://doi.org/10.13131/ARCHEOLOGICADATA-C4V3-E890.

Vergnano, A., D. Franco, A. Merico, F. Pace, S. Uggè, and C. Comina. 2025. "Survey and Sequence Strategies for Full-3D Electrical Resistivity Tomography in Archaeological Sites: A Case Study on a Domus of the Roman Town of Augusta Bagiennorum (NW Italy)." *Archaeological Prospection* 33: 87–107. https://doi.org/10.1002/arp.70013.

Verhoeven, G., and M. Doneus. 2011. "Balancing on the Borderline—A Low-Cost Approach to Visualize the Red-Edge Shift for the Benefit of Aerial Archaeology." *Archaeological Prospection* 18, no. 4: 267–278. https://doi.org/10.1002/arp.420.

Vogel, S., and M. Märker. 2011. "Characterization of the Pre-AD 79 Roman Paleosol South of Pompeii (Italy): Correlation Between Soil Parameter Values and Paleo-Topography." *Geoderma* 160, no. 3–4: 548–558. https://doi.org/10.1016/j.geoderma.2010.11.003.

Vogel, S., and M. Märker. 2012. "Comparison of Pre-AD 79 Roman Paleosols in Two Contrasting Paleo-Topographical Situations Around Pompeii (Italy)." *Geografia Fisica e Dinamica Quaternaria* 35, no. 2: 199–209. https://doi.org/10.4461/GFDQ.2012.35.18.

Waagen, J. 2019. "New Technology and Archaeological Practice. Improving the Primary Archaeological Recording Process in Excavation by Means of UAS Photogrammetry." *Journal of Archaeological Science* 101: 11–20. https://doi.org/10.1016/j.jas.2018.10.011.

Wynn, J. C. 1986. "A Review of Geophysical Methods Used in Archaeology." *Geoarchaeology* 1, no. 3: 245–257. https://doi.org/10.1002/gea.3340010302.

Yu, R., L. Huo, H. Huang, et al. 2022. "Early Detection of Pine Wilt Disease Tree Candidates Using Time-Series of Spectral Signatures." *Frontiers in Plant Science* 13. https://doi.org/10.3389/fpls.2022.1000093.

Zanni, S., and A. De Rosa. 2019. "Remote Sensing Analyses on Sentinel-2 Images: Looking for Roman Roads in Srem Region (Serbia)." *Geosciences* 9, no. 1: 1. https://doi.org/10.3390/geosciences9010025.

Zhang, D., L. Hou, L. Lv, et al. 2025. "Precision Agriculture: Temporal and Spatial Modeling of Wheat Canopy Spectral Characteristics." *Agriculture* 15, no. 3: 3. https://doi.org/10.3390/agriculture15030326.

Zhao, W., G. Tian, E. Forte, et al. 2015. "Advances in GPR Data Acquisition and Analysis for Archaeology." *Geophysical Journal International* 202, no. 1: 62–71. https://doi.org/10.1093/gji/ggv121.

Supporting Information

Additional supporting information can be found online in the Supporting Information section. **Appendix S1:** Insight on topographic survey and reference systems. **Appendix S2:** Multispectral index maps. **Table S1:** NDVI index map (a) and NDRE index map (b) calculated from multispectral orthophoto and their formulations. **Table S2:** EVI 2 index map (a) and BI index map (b) calculated from multispectral orthophoto and their formulations. **Table S3:** NDWI index maps (a) and RN index map (b) calculated from multispectral orthophoto and their formulations. **Appendix S3:** Section 3, geomatics. **Figure S1:** Zoomed views of specific anomalies from Figure 4: (a) linear anomalies perpendicular to the *natatio*; (b) semi-circular anomaly, near the perimeter wall. **Figure S2:** Zoomed views of specific anomalies from Figure 5: (a, b) highlighting vegetation anomalies visible in the optical orthophoto. **Appendix S4:** Section 4, visual interpretation and comparison. **Table S4:** Central area: spectral index-based anomalies, GPR-based anomalies and differences.

10990763, 0, Downloaded from https://onlinelibrary.wiley.com/doi/10.1002/arp.70066 by Valentina Santoro - Politecnico Di Torino Sist. Bibl Del Polit Di Torino , Wiley Online Library on [07/10/2026]. See the Terms and Conditions (https://onlinelibrary.wiley.com/terms-and-conditions) on Wiley Online Library for rules of use; OA articles are governed by the applicable Creative Commons License